AD-A104 514   COMPUTATIONAL MECHANICS CONSULTANTS INC KNOXVILLE TN   F/G 1/3
               A NUMERICAL THREE-DIMENSIONAL TURBULENT SIMULATION OF A SUBSONI--ETC(U)
               JUN 81   A J BAKER, J A ORZECHOWSKI   N62269-79-C-0295
UNCLASSIFIED   NADC-79021-60   NL

1 OF 1
AD A
104514

END
DATE
FILMED
10-81
DTIC

(12)

AD A104514

A NUMERICAL THREE-DIMENSIONAL TURBULENT SIMULATION
OF A SUBSONIC VSTOL JET IN CROSS-FLOW
USING A FINITE ELEMENT ALGORITHM.

By

A. J. /Baker
J. A. /Orzechowski
And
P. D. /Manhardt

Computational Mechanics Consultants, Inc.

3601A Chapman Highway

Knoxville, TN 37920

Jun 1981

Prepared for

Naval Air Development Center

Warminster, PA 18974

81 9 28 016

REPORT DOCUMENTATION PAGE	READ INSTRUCTIONS BEFORE COMPLETING FORM

1. REPORT NUMBER	2. GOVT ACCESSION NO.	3. RECIPIENT'S CATALOG NUMBER
NADC-79021-60	AD-A104 514	

4. TITLE (and Subtitle)	5. TYPE OF REPORT & PERIOD COVERED
A Numerical Three-Dimensional Turbulent Simulation Of A Subsonic VSTOL Jet In Cross-Flow Using A Finite Element Algorithm	FINAL REPORT 9/79-9/80
	6. PERFORMING ORG. REPORT NUMBER

7. AUTHOR(s)	8. CONTRACT OR GRANT NUMBER(s)
A. J. Baker, J. A. Orzechowski and P. D. Manhardt	N62269-79C-0295

9. PERFORMING ORGANIZATION NAME AND ADDRESS	10. PROGRAM ELEMENT, PROJECT, TASK AREA & WORK UNIT NUMBERS
Computational Mechanics Consultants 3601-A Chapman Highway Knoxville, Tennessee 37920	

11. CONTROLLING OFFICE NAME AND ADDRESS	12. REPORT DATE
Naval Air Development Center (3015) Warminster, Pennsylvania 18974	June 1981
	13. NUMBER OF PAGES

14. MONITORING AGENCY NAME & ADDRESS(If different from Controlling Office)	15. SECURITY CLASS. (of this report)
	UNCLASSIFIED
	15a. DECLASSIFICATION/DOWNGRADING SCHEDULE

16. DISTRIBUTION STATEMENT (of this Report)

Approved for public release; distribution unlimited.

17. DISTRIBUTION STATEMENT (of the abstract entered in Block 20, if different from Report)

18. SUPPLEMENTARY NOTES

19. KEY WORDS (Continue on reverse side if necessary and identify by block number)

VSTOL JET
Three-Dimensional Cross-Flow
Turbulent Flow

Finite Element Algorithm
Computer Program
Numerical Solutions

20. ABSTRACT (Continue on reverse side if necessary and identify by block number)
    The purpose of this study, the results of which are reported herein, was to formulate a mathematical model of the basic VSTOL jet, and to validate its appropriateness by performing a series of computational experiments on the discrete analog (numerical) approximation to the mathematical description. Since the VSTOL jet problem is essentially steady, turbulent and fully three-dimensional, the mathematical description must be quite comprehensive. The approach selected was to utilize a continuity-constrained,

DD FORM 1473 EDITION OF 1 NOV 55 IS OBSOLETE
S/N 0102-014-6601

finite element algorithm for solution of the parabolized form of the time-averaged, three-dimensional Navier-Stokes equations (3DPNS). The essential ingredients of this algorithmic description are presented and discussed. A production finite element computer code (COMOC:3DPNS) was utilized to conduct the computational experiments, and the description of problem definition and data deck preparation is contained at the end of the report. The key results of the computational experiments are discussed, regarding the basic causal mechanisms of the VSTOL jet, as well as results for confirmation test cases documenting viability of the constructed computational model.

PREFACE

iii

TABLE OF CONTENTS

LIST OF SYMBOLS

a	boundary condition coefficient
C	coefficient
d	differential
D	jet diameter
e	finite element index
E	mean flow strain rate tensor
f	function of known argument
h	integration step size
k	turbulence kinetic energy; interpolation polynomial degree
ℓ	differential operator; length scale
L	differential operator
M	number of finite elements spanning R^n
n	unit normal vector; dimensionality
N	finite element cardinal basis
p	pressure; iteration index
q	generalized dependent variable
Q	generalized discretized dependent variable
R	domain of elliptic operator
Re	Reynolds number
S	finite element assembly operator
u_i	mean flow velocity vector
$\overline{u_i' u_j'}$	Reynolds stress tensor
U	reference velocity
x_i	Cartesian coordinate system
α	parameter
∂R	boundary of solution domain R^n

δ	Kronecker delta; increment
Δ	increment; element measure
ε	turbulence dissipation function
λ	jet velocity ratio
ν	kinematic viscosity
ρ	density
σ_{ij}	mean flow Stokes stress tensor
ϕ	harmonic function for conservation of mass
Ω	global solution domain

Superscripts:

h	approximation
n	dimension of R
o	initial condition
T	matrix transpose
~	mass-weighted time-average
——	time average
^	unit vector
′	fluctuating component; ordinary derivative

Subscripts:

∞	freestream reference condition
e	finite element domain
i,j,k,ℓ	tensor indices
j	jet reference
n	normal

Notation:

{ }	column matrix
[ ]	square matrix
$\cup$	union
$\cap$	intersection
ε	belongs to
| |	absolute value

LIST OF FIGURES

INTRODUCTION

In the transition from hover to wing-borne flight, a significant portion of VSTOL aircraft lift is furnished by engine thrust. The injection of a high-velocity jet of exhaust (or air), at almost right angles to the aerodynamic surface, and to the cross-flow induced by the aircraft forward flight, produces an extremely complicated three-dimensional flowfield which can significantly impact aerodynamic performance. Since the basic phenomenon of transverse jet injection is so fundamental to VSTOL performance, it is crucially important that a firm understanding of cause and effect be established. The purpose of this project was to ascertain dominant fluid-dynamic mechanisms characterizing the basic VSTOL jet, using a computational simulation of a mathematical description of the associated three-dimensional turbulent flowfield.

Since the transverse jet is fundamental to many physical processes, in addition to VSTOL aircraft, an extensive base of experimental data and linearized theoretical analyses is in existence. The first consequential theoretical study was reported in the dissertation of Chang [1], who employed potential flow theory and bound vortex filament concepts to predict the shape of the separation boundary between a uniform onset flow perpendicular to a cylindrical jet. A series solution yielded the initial roll-up near the jet exit plane. A (hand) numerical solution produced the down-field roll-up, which illustrated evolution to the hallmark horse-shoe cross-sectional shape. The basic concept of application of potential flow theory has been extended and refined to a great extent. Viscous-corrected potential models can now accurately predict gross far-field flow characteristics such as jet centerline trajectory, lateral spread, cross-section shape and mean axial velocity at each cross-section, c.f., [2, 3].

Jordinson [4] conducted pioneering experiments on a round VSTOL jet, that confirmed the horse-shoe cross-section contours predicted by the potential flow models. However, his results also confirmed that the VSTOL jet induced the injection plane boundary layer flow to become entrained into the wake region behind the jet. This action was not predicted by the elementary theory, which prompted the viscous-correction procedures. This action is not characteristic of a jet issued from an isolated orifice [5], and has become recognized as perhaps the consequential contributor to alterations of VSTOL aircraft performance. "Entrainment" is properly interpreted as the total effect of vortex

1

roll-up plus turbulent mixing, while "blockage" describes inviscid flow around an equivalent solid body. The potential flow model equivalent is therefore a cylinder with suction coupled with an impirical accounting for viscous effects.

These observations from Jordinson's data prompted conducting of a wide range of experimental tasks, cf., [6-12]. McMahon and Mosher [8] published photographs of oil flow streaklines on the injection plate, see Figure 1, that provide qualitative evidence of the difference between a VSTOL jet and the equivalent-diameter solid blockage. For the latter, Figure 1a, stagnation points exist both upstream and downstream on the center-line and are connected by an apparent inviscid flow streamline. Outside this streamline, the exterior flow simply responds to the blockage induced by the body. The flow interior to this streamline curves inwards to the centerline and appears to form a closed recirculation zone. Since the plate is impervious, an axial flow must become induced, directed away from the plate and parallel to the solid cylinder for some distance. Thereafter, the shedding of the Karman vortex street probably results.

The streaklines for the circular VSTOL jet, Figure 1b, are consequentially different (note that the concentric circle is part of the experimental apparatus and not a streakline). The upstream stagnation region does not appear consequentially different, indicating blockage-dominance. However, at mid-jet, the surface flow is directed almost radially inwards, in distinct contrast to solid blockage flow. Two streamlines are symmetrically oriented downstream, which separate the complex wake interior flow from the deflected free-stream. The incoming streamlines, which divide the flow region into entrained or deflected segments, intersect the downstream-dividing streamlines symmetrically, and a weak stagnation line appears to connect these two points (essentially on top of the circle).

A close-up from a similar test [9] is shown in Figure 2, which clearly delineates the near wake streakline patterns. A weak stagnation point is indicated about one jet diameter downstream on the symmetry plane, with a transverse streamline separating wake inflow from outflow. The dominant exterior flow deflection streamline is clearly evident, with the blockage flow bifurcating at the intersection with the transverse streamline.

2
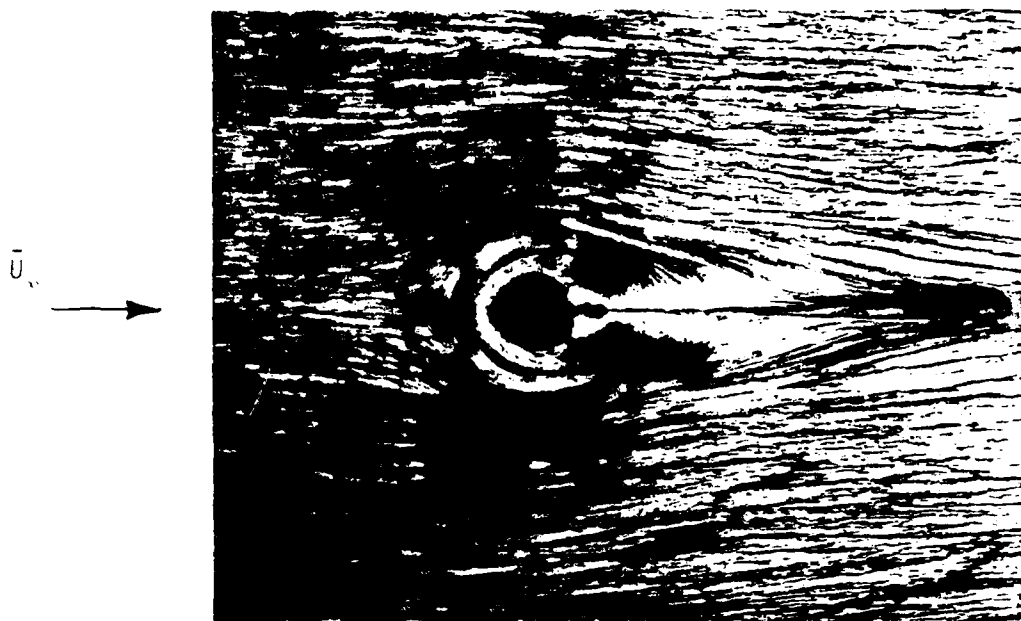
a) Blockage Due To Solid Cylinder
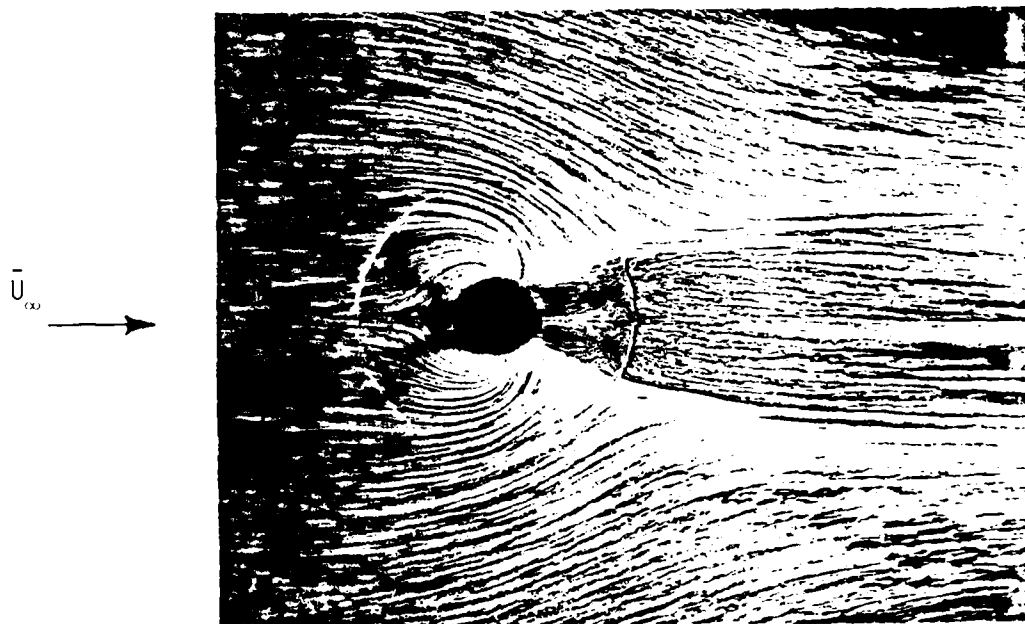
b) Blockage Due To Circular Cross-Section VSTOL Jet, λ = 8

Figure 1   Oil Flow Streaklines On The Injection Plate.
From McMahon And Mosher [8].

3

Additional insight into the basic transverse jet is provided by experimental data obtained using conventional pressure probes in the farfield [10-12]. Figure 3 illustrates the essential VSTOL geometry and coordinate description, and "far-field" is nominally the region downstream of $X_1/D \approx 5$, where D is the jet original diameter. Mosher [10] concludes that, for a circular jet with velocity ratio $4 \leq \lambda \leq 10$, which for incompressible flow is the ratio of jet velocity U_j to the onset freestream velocity U_∞, entrainment is the primary bending mechanism, and becomes more dominant as λ increases. Kamotani and Greber [11] studied the $\lambda = 8$ circular jet and pursued considerable data interpretation. In particular, they determined the locus of plane orientations, along the jet path, with unit normal parallel to the local extremum velocity, ie. the "jet path." In Figure 3, this plane is spanned by the X_2, X_3 coordinates, and the normal vector is parallel to X_1. Their data, plotted in the vertical (YZ) plane, Figure 3, produced the familiar horse-shoe profiles previously determined by Jordinson.

When the local velocity vector is resolved into scalar components in the local transverse plane coordinate system, the jet cross-section shape, and transverse plane counter-rotating vortex flow, immediately become visible. For example, Figure 4 is the symmetric half-plane distribution of axial velocity for $\lambda = 8$, at stations $X_1/D = 7$ and $X_1/D = 23$. The characteristic "kidney" shape of the isovels is clearly illustrated. Since the jet is essentially axisymmetric at the point of injection, a characteristic action of the VSTOL jet appears a preferential erosion of the potential core in the near wake region, producing a double maxima off the symmetry plane. Figure 4c) shows the transverse plane velocity vector distribution at $X_1/D = 23$; the center of the vortex is coincident with the extremum axial velocity, Figure 4b). Transverse velocity data for the $\lambda = 8$ circular jet, confirms existence of the centered double vortex structure as near to injection as $X_1/D = 5.2$, [12]. These data have been examined for similitude; Figure 5 summarizes the minimal data spread for definition of jet trajectory over a range of velocity ratios.

Limitations with conventional probes have precluded gathering of velocity data closer to the injection plane than $X_1/D \approx 5$. (The emergence of the three-color laser Doppler velocimeter will perhaps remove this obstacle.) Additional characterization of the basic VSTOL jet has thus been limited to measurement of pressure distribution on the plate forming the injection plane
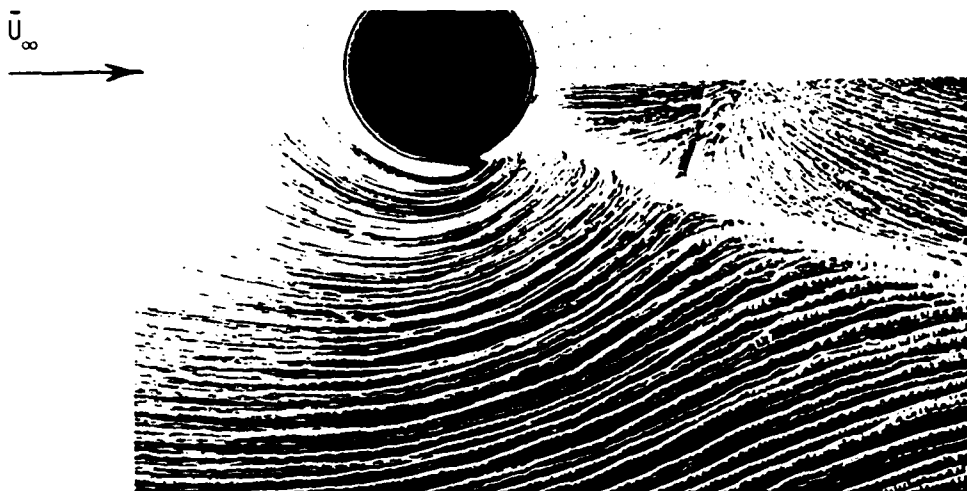
Figure 2   Oil Flow Streaklines For A Circular VSTOL Jet,
From Margason And Fearn [9].
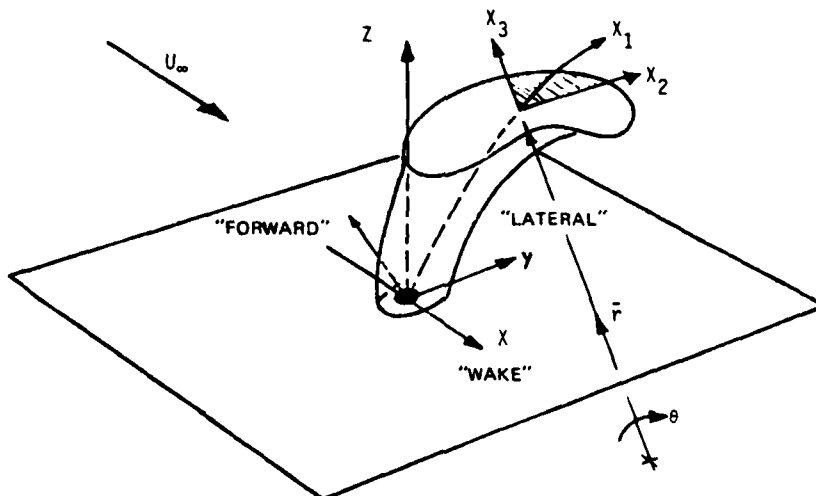
Figure 3   Coordinate Description For VSTOL Jet In A Cross-Flow

Scale ; $\longrightarrow$ $\frac{U_p}{U_0} = 0.5$
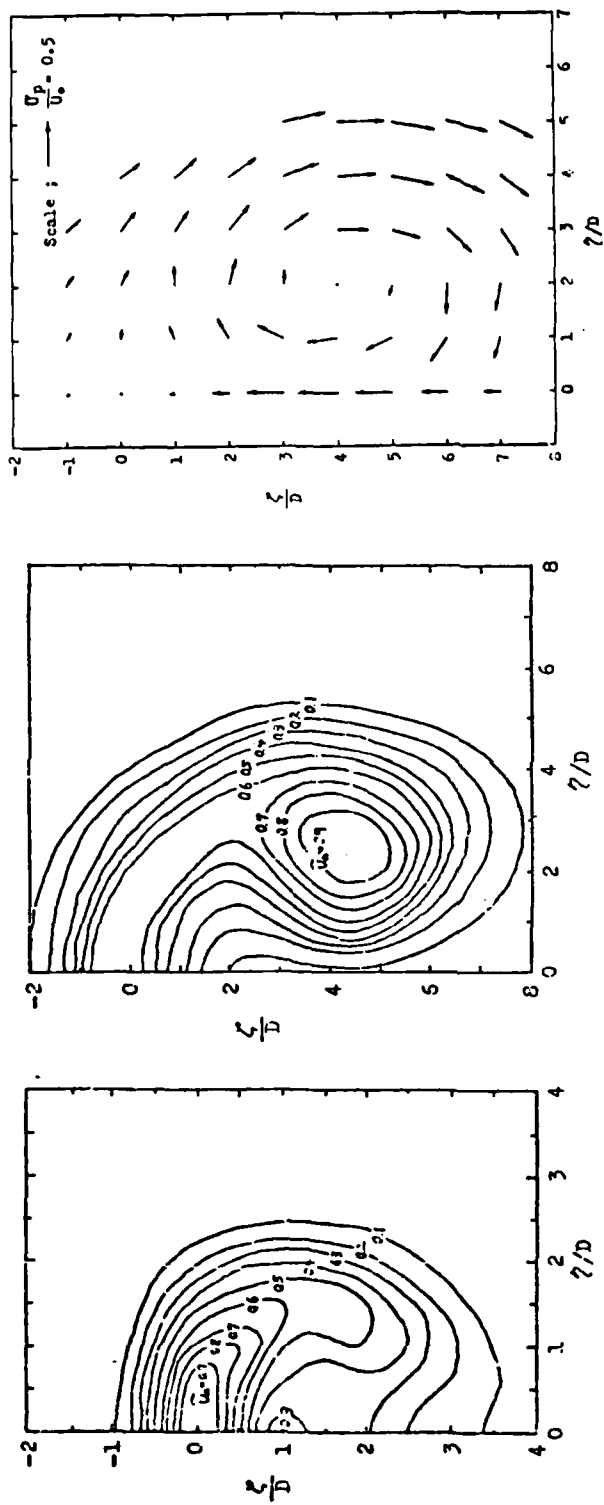
c) Transverse Plane Velocity
   Distribution, $x_1/D = 23$

b) Axial Isovels, $x_1/D = 23$

a) Axial Isovels, $x_1/D = 7.0$

Figure 4   Experimental Velocity Distributions, Circular
            Cross-Section Jet, $\lambda = 8$, From Kamotani and Greber [11]

6

[10-14]. For example, Figure 6 compares two data sets for the injection plate surface pressure coefficient distribution, for the circular jet at $\lambda = 8$. Only the upstream distribution appears analogous to potential flow about a solid cylinder. The extensive low pressure region downstream of mid-jet is a distinctive characteristic of the VSTOL jet, and probably a (the) significant aerodynamic influence, since in reality the injection plane is an aerodynamic surface. Alternative jet cross-sections and shapes modify the details of the associated pressure distribution, see Figure 7, but do not alter the basic character.

A computational simulation of the causal mechanism of the extensive low pressure region is reported [15]. For this analysis, an aerodynamic contour was assumed to exist surrounding the jet, and separating the region of transverse flow affected primarily by blockage, from that dominantly influenced by entrainment. This contour was assumed a porous Joukowski airfoil, with the surface onset (suction) velocity distribution an input parameter of the simulation study. A series of computer experiments were run to optimize agreement of computed pressure coefficient on the airfoil surface, with experimental data on the airfoil image on the injection plate. Figure 8 summarizes the results; the entrainment case, Fig. 8b), clearly produces a large aft region of low pressure, in qualitative agreement with experiment, Fig. 6 and 7b). In comparison to the zero entrainment (solid airfoil) prediction, Fig. 8a) the pressure recovery in the trailing edge region is completely absent.

These experimental data, and the computational experiment, appear to confirm that the large low pressure region is the direct effect of the entrainment action of the basic VSTOL jet. The farfield velocity measurements confirm the preferential wake erosion, of the initially circular jet cross-section, and the evolution of a transverse vortex pair. The axial velocity contours flatten broadside to the onset flow to produce a bluff rather than aerodynamic cross-section. While these data provide a rather comprehensive characterization, the dominant causal influence remains no more well defined than being an interaction between the jet and the cross-flow.

The purpose of this study, the results of which are reported herein, was to formulate a mathematical model of the basic VSTOL jet, and to validate its appropriateness by performing a series of computational experiments on the discrete analog (numerical) approximation to the mathematical description. Since the ideal VSTOL jet problem is essentially incompressible, steady, turbulent and
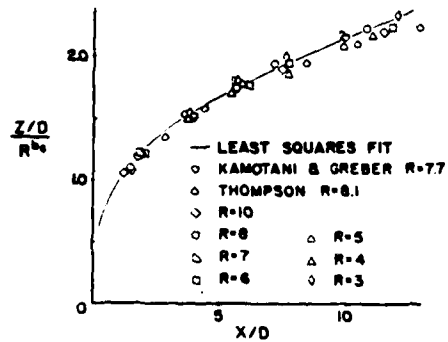
Figure 5   Similitude For Circular Jet Centerline Trajectory,
From Fearn And Weston [12].
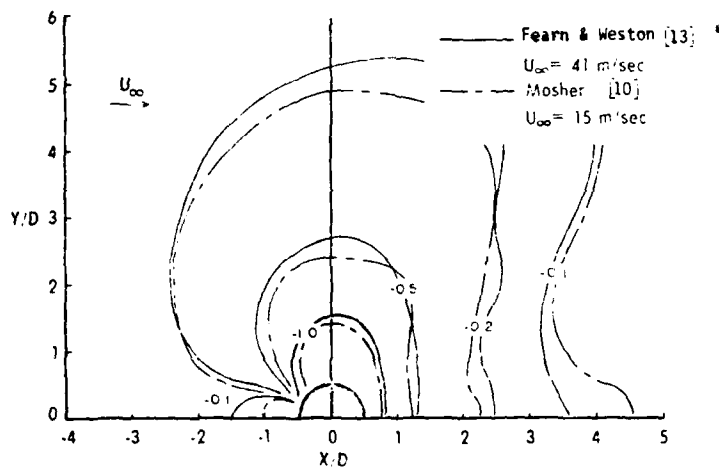
Figure 6   Experimentally Measured Surface Pressure Coefficient
Distributions On Injection Plane, Circular Jet, λ = 8.

fully three-dimensional, the mathematical description must be quite comprehensive. The approach selected was to utilize a continuity-constrained, finite element algorithm for the parabolized form of the time-averaged, three-dimensional Navier-Stokes equations (3DPNS). The essential ingredients of this algorithmic description are discussed in the section on Problem Definition. A production finite element computer code (COMOC:3DPNS) was utilized to conduct the computational experiments, and the description of problem definition and data deck preparation is contained at the end of this report. The key results of the computational experiments are discussed, regarding the basic causal mechanisms of the VSTOL jet, as well as confirmation test case results documenting viability of the constructed computational model.
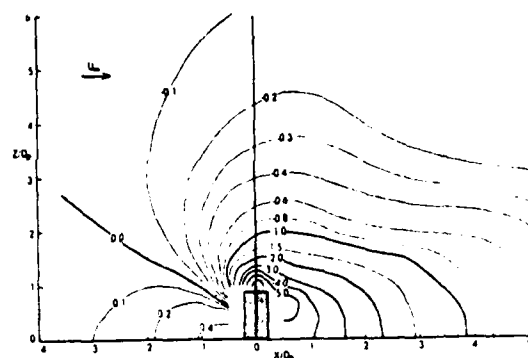
a) Bluff Rectangular
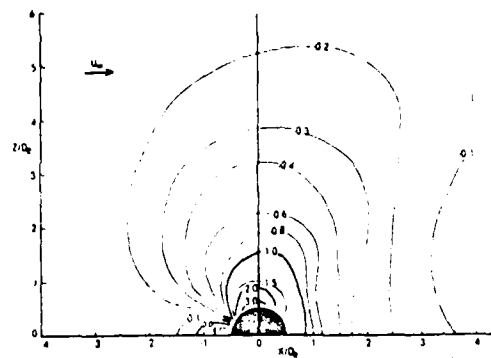
b) Circular
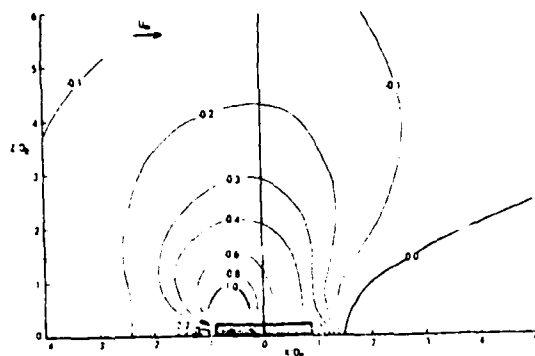
c) Streamline Rectangular

Figure 7   Experimentally Measured Surface Pressure Coefficient
            Distributions On Injection Plane, Various Jets, λ = 4, From [14]

9

a) Solid Blockage With Zero Entrainment

b) Circular Jet With Entrainment, $\lambda = 8$
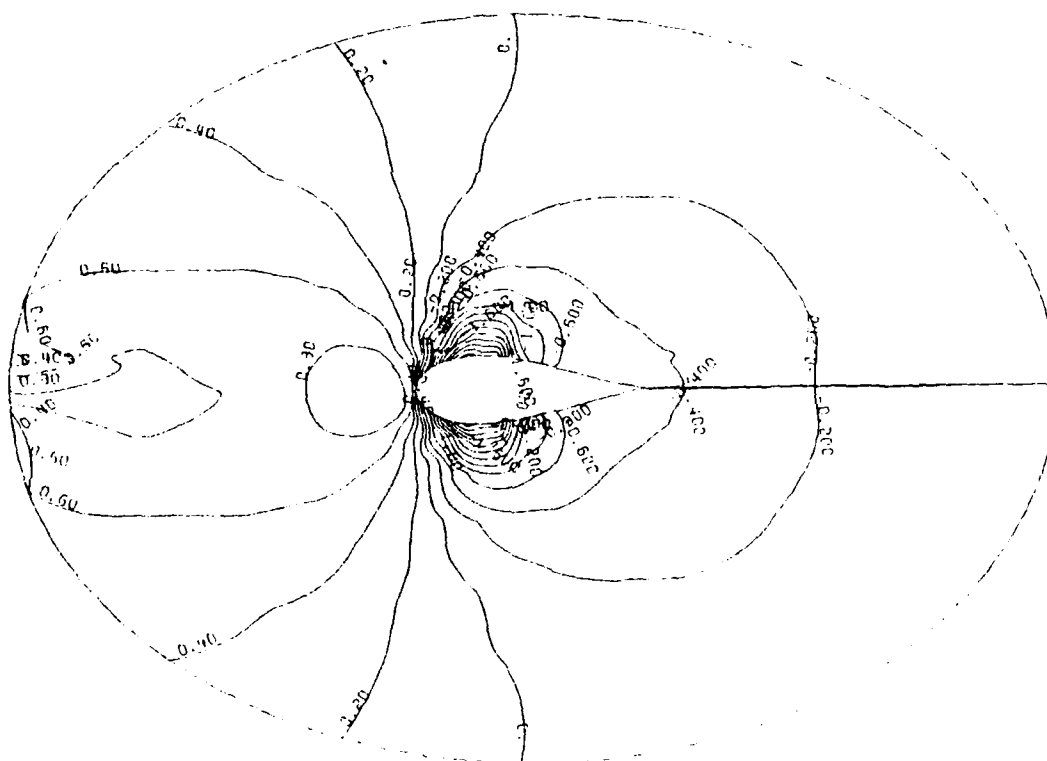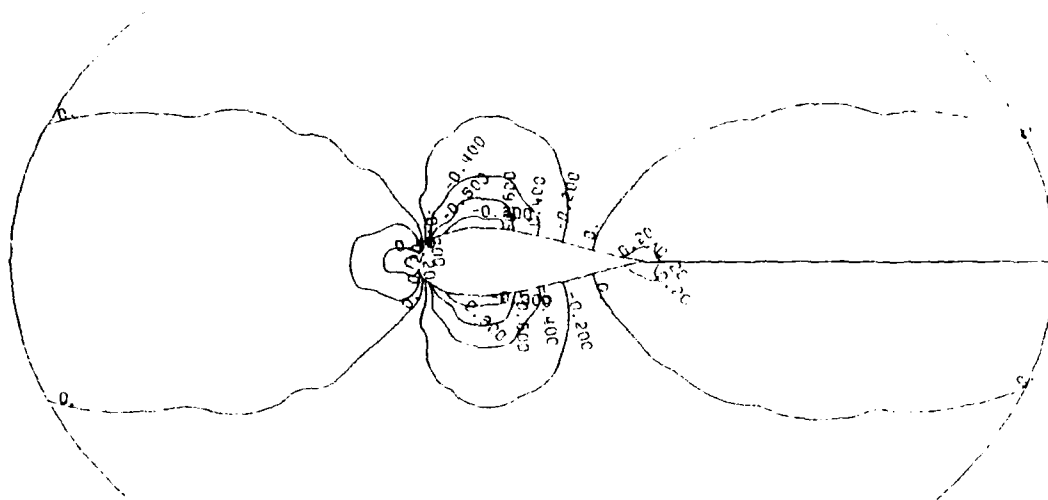
Figure 8   Computed Pressure Coefficient Distribution At Injection Plane,
From Baker, Manhardt And Yen [15]

PROBLEM DEFINITION

Overview

The requirement is to establish a partial differential equation system providing an adequate description of the basic VSTOL jet configuration. As mentioned in the Introduction, the essential features are three-dimensional and turbulent, with the flow basically steady and of constant density. The complete three-dimensional, time-averaged Navier-Stokes equations (3DNS) provide the accurate description; however, their numerical solution is essentially intractible with present computer hardware. The three-dimensional parabolic Navier-Stokes equations (3DPNS) is a simplification of the 3DNS system, that is appropriate for steady flow prediction in aerodynamic configurations wherein the predominant velocity component does not suffer reversal, and where certain other requirements are met. The next level of simplication to 3DNS reduces the problem description to two-dimensional, which is unacceptable. The 3DPNS system is numerically tractible, and therefore has been employed for the computational analysis of the VSTOL jet problem.

This Section presents the construction of the 3DPNS equation system for the VSTOL jet problem, including a turbulence closure model for the Reynolds stress tensor. The finite element numerical solution algorithm for 3DPNS is described, including the differential constraint procedure employed to enforce the (non-parabolic) continuity equation. Documentary numerical results are briefly outlined that validate the theoretical, accuracy and convergence aspects of the resultant computational simulation capability.

Three-Dimensional Parabolic Navier-Stokes Equations

The 3DPNS equation set is a simplification of the steady, three-dimensional time-averaged Navier-Stokes equations. In Cartesian tensor notation, and employing superscript tilde and bar to denote mass-weighted and conventional time-averaging, respectively [16], the conservative equation form for an isoenergetic fluid is

$$L(\bar{\rho}) = \frac{\partial}{\partial x_j}\left[\bar{\rho}\tilde{u}_j\right] = 0 \tag{1}$$

$$L(\bar{\rho}\tilde{u}_i) = \frac{\partial}{\partial x_j}\left[\bar{\rho}\tilde{u}_i\tilde{u}_j + \bar{p}\delta_{ij} + \bar{\rho}\overline{u_i'u_j'} - \bar{\tau}_{ij}\right] = 0 \tag{2}$$

11

$$L(\bar{\rho}k) = \frac{\partial}{\partial x_j}\left[\bar{\rho}\bar{u}_j k + (C_k\frac{k}{\varepsilon}\bar{\rho}\overline{u_i'u_j'} - \bar{\rho}\delta_{ij})\frac{\partial k}{\partial x_i}\right]$$
$$+ \bar{\rho}\overline{u_i'u_j'}\frac{\partial \bar{u}_i}{\partial x_j} + \bar{\rho}\varepsilon = 0 \tag{3}$$

$$L(\bar{\rho}\varepsilon) = \frac{\partial}{\partial x_j}\left[\bar{\rho}\bar{u}_j\varepsilon + C_\varepsilon\frac{k}{\varepsilon}\bar{\rho}\overline{u_i'u_j'}\frac{\partial \varepsilon}{\partial x_j}\right] + C_\varepsilon^1\overline{u_i'u_j'}\frac{\varepsilon}{k}\frac{\partial \bar{u}_i}{\partial x_j}$$
$$+C_\varepsilon^2\frac{\bar{\rho}\varepsilon^2}{k} = 0 \tag{4}$$

In equations 1-2, $\bar{\rho}$ is (constant) density, $\bar{u}_j$ is the mean velocity vector, $\bar{p}$ is pressure, δ_{ij} is the Kronecker delta. The Stokes stress tensor $\bar{\sigma}_{ij}$ is defined in terms of the Reynolds number Re as

$$\bar{\sigma}_{ij} = \bar{\rho}\bar{\nu}(\tilde{E}_{ij} - \frac{2}{3}\varepsilon_{ij}\tilde{E}_{kk})/Re \tag{5}$$

and $\bar{\rho}\overline{u_i'u_j'}$ is the Reynolds stress tensor. The fluid kinematic viscosity is $\bar{\nu}$, and $\tilde{E}_{ij}$ is the mean flow strain rate tensor

$$\tilde{E}_{ij} \equiv \frac{\partial \bar{u}_i}{\partial x_j} + \frac{\partial \bar{u}_j}{\partial x_i} \tag{6}$$

Equations 3-4 are the transport equations for turbulent kinetic energy and isotropic dissipation function, as obtained using the closure model of Launder, Reece and Rodi [17] for the pressure-strain and triple correlations, and

$$k \equiv \tfrac{1}{2}\overline{u_i'u_i'} \tag{7}$$

$$\varepsilon \equiv \frac{2\bar{\nu}}{3}\left[\overline{\frac{\partial u_i}{\partial x_j}\frac{\partial u_i}{\partial x_k}}\right]\delta_{jk} \tag{8}$$

The various coefficients C_β^α are model constants, Hanjalic and Launder [18].

The parabolic Navier-Stokes equation set is derived from equations 1-4 assuming the ratio of extremum transverse mean velocity component to downstream (axial) component is less than unity, and that:

12

1. the downstream velocity component suffers no reversal,

2. diffusive transport processes in the downstream direction are higher-order, hence negligible, and

3. the overall elliptic character of the parent three-dimensional Navier-Stokes equation can become enforced through construction of a suitable pressure field.

Viewing Figure 3, for the VSTOL jet problem, the x_1 (curvilinear) coordinate defines the predominant mean flow direction, with scalar velocity component $\tilde{u}_1$ of order unity, i.e., $O(1)$. Hence, assume $O(\tilde{u}_2) \approx O(\delta) \sim O(\tilde{u}_3)$ and $O(\delta) < O(1)$. Then, the continuity equation 1 asserts that the downstream variation in $\tilde{u}_1$ must be of order equal to appropriate transverse plane variations of $\tilde{u}_2$ and $\tilde{u}_3$; hence, for $\frac{\partial}{\partial x_1} \approx O(1)$, $\frac{\partial}{\partial x_2} \approx O(\delta^{-1}) \approx \frac{\partial}{\partial x_3}$.

Determination of the relative order of terms in the momentum equations 2 is straightforward. For the $\tilde{u}_1$ equation, since $O(\overline{\rho u_i' u_j'})$ must be $O(\delta)$, the term $\frac{\partial}{\partial x_1} (\overline{\rho u_1' u_1'})$ is higher order and discarded. The assumption that the x_1 - diffusion is negligible permits setting $\frac{\partial}{\partial x_1} (E_{11}) \equiv 0$; further, $\frac{\partial}{\partial x_2} \left(\frac{\partial \tilde{u}_2}{\partial x_1} \right) \approx O(\delta)$ $\approx \frac{\partial}{\partial x_3} \left(\frac{\partial \tilde{u}_2}{\partial x_1} \right)$. Deletion of these terms is the fundamental step to the parabolic approximation, as it removes the elliptic character in the downstream direction. The convection term $\frac{\partial}{\partial x_1} (\overline{\rho} \tilde{u}_1 \tilde{u}_1)$ instills the initial value form that permits marching the solution for $\tilde{u}_1$ in the downstream direction. The final 3DPNS form, denoted $L^P(.)$, for the $\tilde{u}_1$ momentum equation is

$$L^P(\overline{\rho}\tilde{u}_1) \equiv \frac{\partial}{\partial x_1} (\overline{\rho}\tilde{u}_1\tilde{u}_1) + \frac{\partial \overline{p}}{\partial x_1} + \frac{\partial}{\partial x_2} \left[\overline{u_1' u_2'} - \overline{\sigma}_{12} \right]$$

$$+ \frac{\partial}{\partial x_3} \left[\overline{\rho u_1' u_3'} - \overline{\sigma}_{13} \right] = 0 \tag{9}$$

As a final note, should x_j correspond to a curvilinear coordinate description, the derivatives expressed in equation 9 become the covariant derivative.

In agreement with the parabolic concept, the order of pressure variation in the transverse plane must be determined by the lowest order terms appearing in equation 2 written on $\tilde{u}_2$ and $\tilde{u}_3$. Each transverse derivative of $\overline{\rho u_2' u_j'}$ and $\overline{\rho u_3' u_j'}$ is $O(1)$, while all other terms are $O(\delta)$ and higher.

13

The resultant three-dimensional parabolic approximation is made numerically tractible by taking the divergence of the approximation to equation 2. Retaining the higher-order convection and laminar diffusion terms for generality, the 3DPNS equivalent of both transverse momentum equations is [19],

$$L(\bar{p}) = \frac{\partial^2 \bar{p}}{\partial x_\ell^2} + \frac{\partial^2}{\partial x_j \partial x_\ell}\left[\bar{\rho}\bar{u}_\ell\bar{u}_j + \overline{\rho u_\ell' u_j'} - \bar{\tau}_{\ell j}\right] = 0 \tag{10}$$

which defines the 3DPNS limited index summation convention, $1 \le (i,j) \le 3$, $2 \le \ell \le 3$.

Equation 10 defines an elliptic boundary value problem for determination of pressure distributions in the transverse plane. The pressure field that satisfies this Poisson equation consists of complementary and particular solutions.

$$\bar{p}(x_i) = p_c(x_i) + p_p(x_i) \tag{11}$$

The complementary solution is assumed to satisfy the convection phenomena,

$$L(p_c) = \frac{\partial^2 p_c}{\partial x_\ell^2} + \frac{\partial^2(\bar{\rho}\bar{u}_\ell\bar{u}_j)}{\partial x_j \partial x_\ell} = 0 \tag{12}$$

subject to the Dirichlet boundary conditions known for $p(x_1, x_\ell)$. Elsewhere, an appropriate boundary condition for p_c is homogeneous Neumann. The particular pressure p_p satisfies equation 10, less the convection term, subject to homogeneous Dirichlet boundary conditions on boundary segments where p_c is known.

The critical aspect affecting application of the 3DPNS equation set to analysis of the VSTOL jet, is knowledge of the boundary values for $\bar{p}$ (x_1, x_ℓ), as required via assumption 3 of the 3DPNS argument. Viewing Figure 3, the VSTOL jet is a fully three-dimensional problem with elliptic coupling throughout in its entirety. However, see Figure 5, the trajectory of the jet for the first few jet diameters away from the injection plane is nominally vertical. Hence, if the 'computational box" surrounding the jet and the near field flow is sufficiently large in lateral (X,Y) extent, it is fair to assume that the potential flow pressure exists on the box boundaries, and for some vertical distance (parallel to the Z axis). Therefore, the validity of the 3DPNS analysis is expected to be limited to a region close to the injection plate surface, eg., $0 < x_1/D < 4$, provided the lateral boundaries are sufficiently remote. For the analyses reported herein, these boundaries of the 3DPNS

simulation were placed at $|x_\ell|/D \approx 3$. The jet path was assumed straight and perpendicular to the plane. The complementary pressure solution boundary condition $\bar{p}$, on the upstream and lateral side boundaries, were set by the farfield potential solution for flow about a cylinder. The complementary pressure $\bar{p}_c$ at the outflow boundary was determined using Bernoulli's equation, which admitted reversal of the transverse flow and was compatible with the lateral farfield potential solution.

Reynolds Stress Closure Model for 3DPNS

A closure model for the kinematic Reynolds stress $-\overline{u_i'u_j'}$, appearing in equations 3-4 is required to complete the 3DPNS order of magnitude analysis. A stress-strain rate constitutive equation, Baker, et. al. [20] establishes the lead terms of the kinematic form as

$$-\overline{u_i'u_j'} = -k\alpha_{ij} + C_4\frac{k^2}{\varepsilon}\tilde{E}_{ij} + C_2 C_4\frac{k^3}{\varepsilon^2}\tilde{E}_{ik}\tilde{E}_{kj} + \cdots \tag{13}$$

$\tilde{E}_{ij}$ remains the symmetric mean flow strain-rate tensor given in equation 6. This expansion results from re-expression of triple correlations within the *Reynolds stress transport equation* using the model of Launder, Reece and Rodi [17], and is a generalization of the original analysis by Gessner and Emery [21]. In equation 13, α_{ij} is a diagonal tensor in principal coordinates.

$$\alpha_{ij} \equiv \frac{1}{3k}(\overline{u_k'u_k'})a_i\delta_{ij} \tag{14}$$

The a_i are coefficients admitting anisotropy, where $a_1 \equiv C_1$, and $a_2 \equiv C_3 \equiv a_3$. The C_α are defined as, see Launder et. al. [17].

$$C_1 \equiv \frac{22(C_{01} - 1) - 6(4C_{02} - 5)}{33(C_{01} - 2C_{02})}$$

$$C_2 \equiv \frac{4(3C_{02} - 1)}{11(C_{01} - 2C_{02})}$$

$$C_3 \equiv \frac{22(C_{01} - 1) - 12(3C_{02} - 1)}{33(C_{01} - 2C_{02})}$$

$$C_4 \equiv \frac{44C_{02} - 22C_{01}C_{02} - 128C_{02} - 36C_{02}^2 + 10}{165(C_{01} - 2C_{02})^2} \tag{15}$$

15

where C_{01} and C_{02} are "universal" empirical constants. Suggested values are $C_{01} \approx 2.8$ and $C_{02} \sim 0.45$, Hanjalic and Launder [18]. In rectangular Cartesian coordinates, and retaining terms of the first two orders of significance, the kinematic Reynolds stress scalar components are

$$O(\delta) \qquad\qquad\qquad O(\delta^2)$$

$$-\overline{u_1' u_1'} = C_1 k - C_2 C_4 \frac{k^3}{\varepsilon^2}\left[\left(\frac{\partial \tilde{u}_1}{\partial x_2}\right)^2 + \left(\frac{\partial \tilde{u}_1}{\partial x_3}\right)^2\right] - 2C_4\frac{k^2}{\varepsilon}\left[\frac{\partial \tilde{u}_1}{\partial x_1}\right]$$

$$-\overline{u_2' u_2'} = C_3 k - C_2 C_4 \frac{k^3}{\varepsilon^2}\left[\frac{\partial \tilde{u}_1}{\partial x_2}\right]^2 - 2C_4\frac{k^2}{\varepsilon}\left[\frac{\partial \tilde{u}_2}{\partial x_2}\right]$$

$$-\overline{u_3' u_3'} = C_3 k - C_2 C_4 \frac{k^3}{\varepsilon^2}\left[\frac{\partial \tilde{u}_1}{\partial x_3}\right]^2 - 2C_4\frac{k^2}{\varepsilon}\left[\frac{\partial \tilde{u}_3}{\partial x_3}\right]$$

$$-\overline{u_1' u_2'} = - C_4\frac{k^2}{\varepsilon}\left[\frac{\partial \tilde{u}_1}{\partial x_2}\right] - C_2 C_4 \frac{k^3}{\varepsilon^2}\left[\frac{\partial \tilde{u}_1}{\partial x_3}\left(\frac{\partial \tilde{u}_2}{\partial x_3} + \frac{\partial \tilde{u}_3}{\partial x_2}\right)\right.$$
$$\left. + 2\frac{\partial \tilde{u}_1}{\partial x_2}\left(\frac{\partial \tilde{u}_1}{\partial x_1} + \frac{\partial \tilde{u}_2}{\partial x_2}\right)\right]$$

$$-\overline{u_1' u_3'} = - C_4\frac{k^2}{\varepsilon}\left[\frac{\partial \tilde{u}_1}{\partial x_3}\right] - C_2 C_4 \frac{k^3}{\varepsilon^2}\left[\frac{\partial \tilde{u}_1}{\partial x_2}\left(\frac{\partial \tilde{u}_2}{\partial x_3} + \frac{\partial \tilde{u}_3}{\partial x_2}\right)\right.$$
$$\left. + 2\frac{\partial \tilde{u}_1}{\partial x_3}\left(\frac{\partial \tilde{u}_1}{\partial x_1} + \frac{\partial \tilde{u}_3}{\partial x_3}\right)\right]$$

$$-\overline{u_2' u_3'} = - C_2 C_4 \frac{k^3}{\varepsilon^2}\left[\frac{\partial \tilde{u}_1}{\partial x_2}\frac{\partial \tilde{u}_1}{\partial x_3}\right] - C_4\frac{k^2}{\varepsilon}\left[\frac{\partial \tilde{u}_2}{\partial x_3} + \frac{\partial \tilde{u}_3}{\partial x_2}\right] \qquad (16)$$

With equation 16, the ordering of terms in equations 3-4 can be completed to establish the appropriate 3DPNS approximation as, $1 \le i \le 3$, $2 \le \ell \le 3$,

$$L^P(k) = \frac{\partial}{\partial x_i}(\tilde{\rho}\tilde{u}_i k) + \frac{\partial}{\partial x_i}\left[\tilde{\rho}(C_k\frac{k}{\varepsilon}\overline{u_i' u_\ell'} - \tilde{\nu})\frac{\partial k}{\partial x_\ell}\right]$$
$$+ \tilde{\rho}\,\overline{u_i' u_\ell'}\frac{\partial \tilde{u}_1}{\partial x_\ell} + \tilde{\rho}\varepsilon = 0 \qquad (17)$$

$$L^P(\varepsilon) = \frac{\partial}{\partial x_i}(\rho \hat{u}_i \varepsilon) + \frac{\partial}{\partial x_i}\left[C_\varepsilon\frac{k}{\varepsilon}\overline{u_i' u_\ell'}\frac{\partial \varepsilon}{\partial x_\ell}\right]$$
$$+ C_\varepsilon^1\,\overline{\rho u_i' u_\ell'}\frac{\varepsilon}{k}\frac{\partial \tilde{u}_1}{\partial x_\ell} + C_\varepsilon^2\,\tilde{\rho}\frac{\varepsilon^2}{k} = 0 \qquad (18)$$

16

Finite Element Solution Algorithm

The consistently ordered 3DPNS equation system has been identified. For the dependent variable set $q_j(x_i) \equiv \{q\} = \{\tilde{u}_1, \tilde{u}_2, \tilde{u}_3, \bar{p}, k, \epsilon\}^T$, the governing system includes equations 1, 9, 10, 13, 17 and 18. Equations 9, 10, 17 and 18 exhibit the initial value term that permits the space-marching of 3DPNS. Equation 13 exhibits elliptic boundary value character with parametric initial-value dependence. The continuity equation 1 solution will become recast and utilized as a differential constraint.

The generalized form of the 3DPNS description is

$$L^p(q_j) = \frac{\partial}{\partial x_1}(\tilde{u}_1 q_j) + \frac{\partial}{\partial x}\left[\tilde{u}_\ell q_j + f_{\ell j}\right] + s_j = 0 \tag{19}$$

where $f_{\ell j}$ and s_j are specified non-linear functions of their arguments, as determined by the index j. The solution domain Ω is defined as the product of R^2 and x_1, for all elements of x_1 belonging to the open interval measured from $x_1(0)$, i.e.,

$$\Omega \equiv R^2 \times x_1 = \{(x_\ell, x_1): x_\ell \epsilon R^2 \text{ and } x_1 \epsilon [x_1(0), x_1) \tag{20}$$

The boundary $\partial\Omega$ is the product of the boundary ∂R of R^2 and x_1, $\partial\Omega \equiv \partial R \times x_1$. Thereupon, the generalized differential boundary constraint is

$$\ell(q_j) = a_1 q_j + a_2 \frac{\partial}{\partial x_i} q_j \hat{n}_i + a_3 = 0 \tag{21}$$

where the a_i are specified coefficients and $\hat{n}_i$ is the outwards pointing unit normal vector. Finally, an initial distribution for q_j on $\Omega_0 \equiv R^2 \times x_1(0)$ is required.

$$q_j(x_\ell, x_1) \equiv q_j^o(x_\ell) \tag{22}$$

The finite element numerical solution algorithm for equations 19-22 defines the approximation $q_j^h(x_\ell, x_1)$, to the (unknown) exact solution $q_j(x_\ell, x_1)$, which is constructed from members of a finite dimensional subspace of $H_0^1(\Omega)$, the Hilbert space of all functions possessing square integrable first derivatives and satisfying equation 21. Hence,

$$q_j(x_\ell, x_1) \approx q_j^h(x_\ell, x_1) \equiv \sum_{e=1}^{M} q_j^e(x_\ell, x_1) \tag{23}$$

17

and the elemental approximation is defined as

$$q_j^e(x_\ell, x_1) \equiv \{N_k(x_\ell)\}^T \{QJ(x_1)\}_e \tag{24}$$

In equations 23-24, $j(J)$ is a free index denoting members of $\{q^h\}$, and sub-
or super-script e denotes pertaining to the $e^{\underline{th}}$ finite element, $\Omega_e \equiv R_e^2 \times x_1$.
The elements of the row matrix $\{N_k(x_\ell)\}^T$ are (linear, $k = 1$) polynomials on x_ℓ,
$2 \leq \ell \leq 3$, constructed to form a cardinal basis [22].

The functional algorithm requirement is to render the error in q_j^h minimum
is some norm. This is accomplished using the finite element algorithm, by re-
quiring the generated errors $L^p(q_j^h)$ and $\ell(q_j^h)$ to be orthogonal to the function
space employed to define q_j^h, and that the discrete approximation $L^p(\bar\rho^h)$ to
the continuity equation 1 be enforced as a differential constraint. Identify-
ing the multiplier set β_i, these constraints are combined [22] to form the
theoretical statement of the finite element solution algorithm as

$$\int_{R^2}\{N_k\}L^p(q_j^h)d\vec{x} + \beta_i\int_{\partial R}\{N_k\}\ell(q_j^h)d\vec{x} + \vec{\beta}_2 \cdot \int_{R^2}\vec{\nabla}\{N_k\}L^p(\bar\rho^h)d\vec{x} \equiv \{0\} \tag{25}$$

Equation 25 defines a system of ordinary differential equations written
on the jet direction x_1.

$$[C]\{QJ\}' + [U]\{QJ\} + [FLJ]\{QL\} + \{SJ\} = \{0\} \tag{26}$$

Using the trapezoidal integration rule, and substituting equation 25 yields,

$$\{FJ\} \equiv \{QJ\}_{j+1} - \{QJ\}_j - \frac{\Delta x_1}{2}[\{QJ\}'_{j+1} + \{QJ\}'_j] \equiv \{0\} \tag{27}$$

which defines a system of non-linear algebraic equations for determination of
the elements of $\{QJ(x_1)\}$. The Newton iteration algorithm for equation 27 is

$$[J(FJ)]_{j+1}^p \{\delta QJ\}_{j+1}^{p+1} = -\{FJ\}_{j+1}^p \tag{28}$$

written on the iteration vector $\{\delta QI\}$, where

$$\{QJ\}_{j+1}^{p+1} \equiv \{QJ\}_{j+1}^p + \{\delta J\}_{j+1}^{p+1} \tag{29}$$

The remaining issue is the non-parabolic continuity equation 1, which
governs first-order effects on the mean velocity field $\tilde u_i$. Since the formal

18

3DPNS momentum equation 9 is written on $\tilde{u}_1$ only, $\tilde{u}_k \equiv \{\tilde{u}_2, \tilde{u}_3\}$ is required to be determined from the solution of equation 1. This is accomplished in the finite element algorithm formulation by enforcing a measure of the solution of equation 1 as a differential constraint on the solution of the (higher-order) 3DPNS approximation to equation 2 written on $\tilde{u}_\ell$. Retaining the highest two orders of terms, the 3DPNS order of magnitude analysis for transverse momentum equations yields

$$L^p(\rho\tilde{u}_k) = \frac{\partial}{\partial x_1}\left[\bar{\rho}\tilde{u}_1\tilde{u}_k + \overline{\rho u_1 u_k'}\right]$$

$$+ \frac{\partial}{\partial x_\ell}\left[\bar{\rho}\tilde{u}_\ell\tilde{u}_k + \overline{\rho u_\ell' u_k'} + \bar{p}\delta_{k\ell} - \bar{\sigma}_{k\ell}\right] = 0$$

(30)

Note that equation 30 is of the form of equation 19, and employs the 3DPNS limited index $2 \leq k \leq 3$. The middle two terms in the second bracket are $O(1)$, while the remaining terms are all $O(\delta)$. The boundary condition statement 21 is appropriate, upon the retention of terms of $O(\delta^2)$ in the Reynolds stress equation. The initial condition statement for equations 30 is expressed in equation 22.

The finite element algorithm statement for equation 30 is given by equation 25, upon specification of the form of the term modified by β_2. The theoretical concept, borrowed from the variational calculus [22], is to enforce a measure of the continuity equation (solution) as a differential constraint on solution of the transverse momentum equations. This solution measure must span R^2, and must vanish as continuity becomes satisfied; the appropriate measure is the harmonic function $\phi(x_\ell)$, the solution to the Poisson equation

$$L^p(\phi) \equiv \frac{\partial^2\phi}{\partial x_\ell^2} - \frac{\partial}{\partial x_i}(\bar{\rho}\tilde{u}_i) \equiv 0$$

(31)

The boundary conditions for ϕ are homogeneous Dirichlet everywhere at farfield. Equation 31 becomes homogeneous as the continuity equation 1 becomes satisfied, and ϕ becomes null as a consequence of the boundary condition specifications. A detailed discussion of the algorithmic embodiment of the differential constraint concept is given in [22].

Documentary Results

The finite element, differential-constraint numerical solution algorithm
for the 3DPNS equation system 1, 9, 10, 13, 17, 18, 30 and 31, for a turbulent,
subsonic three-dimensional analysis in bounded, semi-bounded and fully unbounded
solution domains Ω , is operational in the COMOC:3DPNS computer program. A
latter report Section presents the detailed data deck set-up procedure for the
VSTOL jet simulation study. Additional documentation on data preparation for
COMOC:3DPNS will become available [23].

Documentation of theoretical concepts, and numerical tests to evaluate
accuracy and convergence are reported elsewhere, cf. [19], [22]. As becomes
apparent in the results discussion, the essential requirements for the 3DPNS
VSTOL simulation are robust enforcement of (the non-parabolic) continuity
equation, and accounting of the turbulence interaction between the jet and the
cross-flow.

Test case results attest to excellent performance of the algorithm in COMOC:
3DPNS in each area. The two-dimensional form of the 3DPNS algorithm, ie., 2DPNS,
must accurately predict ducted and boundary layer flows, as well as free shear
layers. Table 1, from [19], summarizes the comparison between the direct
boundary layer solution, and the continuity-constraint 2DPNS algorithm results,
for a laminar, incompressible zero-pressure gradient boundary layer flow. The
digit of significance ranges over six digits (10^6) and the agreement is excel-
lent. The 2DPNS solution is actually more accurate near the wall (x_2/δ =
0.0009), where a better approximation to vanishing x_2- derivative is achieved.

The intrinsic global measure of error in exact conservation of mass is the
energy norm,

$$E(\phi^h,\phi^h) \equiv \int_{R^n} \frac{\partial \phi^h}{\partial x_\ell} \frac{\partial \phi^h}{\partial x_\ell} d\vec{x} \tag{32}$$

where ϕ^h is the approximate solution to equation 31. The evaluation of $E(\cdot,\cdot)$
decreases monotonically during iteration at j+1, and for this laminar flow
check case, $E(\cdot,\cdot) \leq 10^{-8}$ for algorithm convergence at $\varepsilon = 10^{-5}$. The corres-
ponding levels for a turbulent boundary layer or ducted flow are $E(\cdot,\cdot) < 10^{-5}$
for $\varepsilon = 10^{-4}$ [19].

20

The critical evaluation of the Reynolds stress closure system, *equations*
13-16, is also reported in [19]. For three-dimensional, incompressible flow in
a straight channel of uniform rectangular cross-section, an axial vortex pair
is induced in each corner for a turbulent flow, while none is generated if the
flow is laminar. The results of the 3DPNS simulation confirm these assertions
on both counts. In particular, generation of the counter-rotating vortex pair
for turbulent flow was computationally traced to non-isotropy of the transverse
plane normal stresses $-\overline{u_\ell u_\ell}$. Viewing equation 16, this influence is produced
by a term of $O(\delta^2)$, which confirms the importance of a consistent ordering pro-
cedure. Figure 9 shows the excellent qualitative comparison of the transverse
plane velocity vector distribution as produced by COMOC:3DPNS [19], and the
experimental data of Melling and Whitelaw [24].

Table 1

Transverse Velocity Distributions, $u_2(x_2) \times 10^3$

Laminar Incompressible Boundary Layer

Coordinate (x_2/δ)	Boundary Layer Solution	Continuity Constraint Solution
0.0	.0	.0
0.0009	.0000011	.0000001
0.0021	.0000054	.0000030
0.0035	.0000149	.0000114
⋮	⋮	⋮
0.0095	.00011	.00011
⋮	⋮	⋮
0.031	.00118	.00118
⋮	⋮	⋮
0.10	.0128	.0127
⋮	⋮	⋮
0.67	.139	.138
⋮	⋮	⋮
1.0	.218	.218
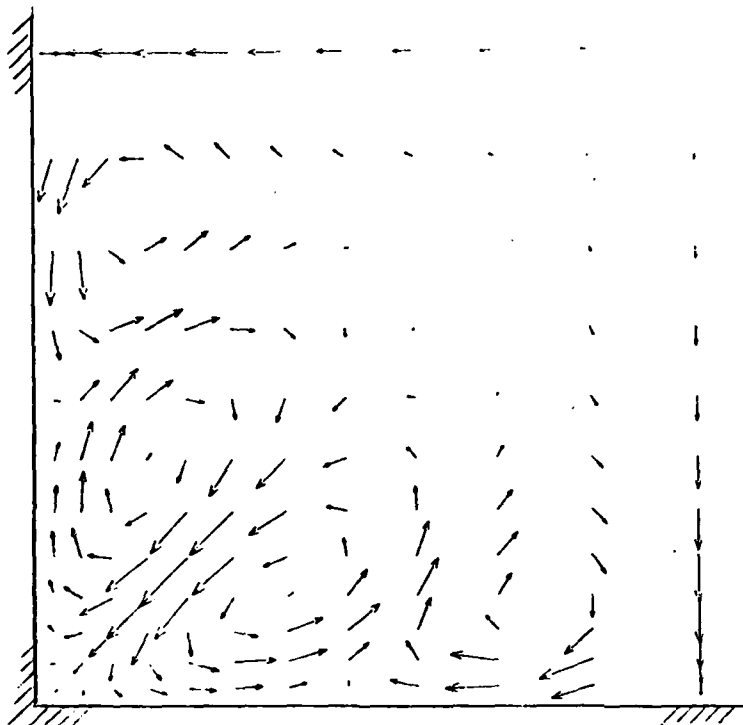
a) $x_1/C = 30.0$

$u_i' u_j'$ Model [19]

$\longrightarrow$ $\tilde{U}/U1 = 0.003$
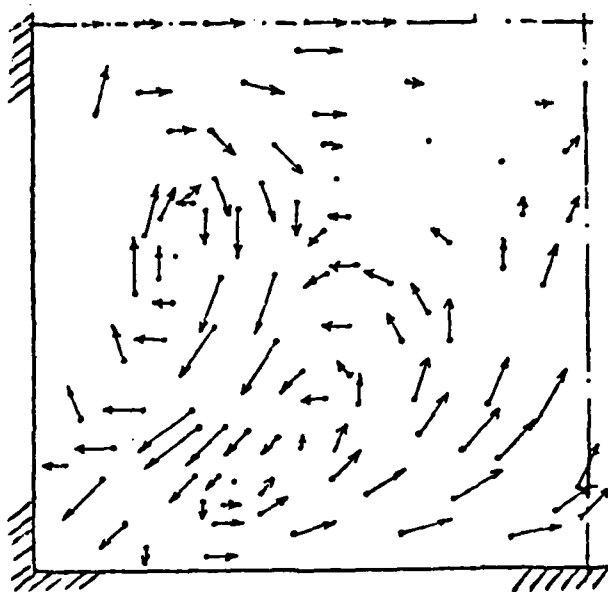
b) $x_1/C = 37.0$

Experiment [14]

$\longrightarrow$ $\tilde{U}/U1 = 0.01$

Figure 9 Computed And Experimental Data Comparison For $\tilde{u}_\ell$, Turbulent Flow In A Rectangular Cross-Section Duct.

RESULTS AND DISCUSSION

Overview

The requirement of the 3DPNS computational simulation of the VSTOL jet is to assess fluid dynamic factors dominating formation of the counter-rotating axial vortex apir, see Figure 6, and entrainment of the cross-flow into the jet wake region, cf. Figures 2-3. The 3DPNS solution domain was defined as the symmetric half-plane, with the circular jet located mid-domain, Figure 10a. For reference, Figure 10b) is the transverse plane potential velocity vector distribution used to initialize $\tilde{u}_\ell(x_1(o), x_\ell)$ at the nodes of $\Omega(o)$. The tail of each vector is at a node, the non-uniform discretization is constituted of $M = 576$ triangular finite element domains R_e^2. Using this discretization, COMOC: 3DPNS required approximately 200,000 words of central memory to solve for eight degrees of freedom/node, using the described implicit algorithm, equations 26-29. No exterior memory was utilized.

Boundary and Initial Conditions

The computational simulation requires solution of a non-linear system of ordinary differential equations. Hence, the members $\tilde{u}_1$, $\tilde{u}_\ell$, k and ε, must be defined initially at the nodes of $\Omega(0)$. Secondly, since the finite element algorithm statement has transformed the elliptic boundary value character of the 3DPNS equations, boundary conditions on all members of $\{QI(x_1)\}$ are re-quired specified everywhere on $\partial\Omega = \partial R^2 \times x_1$. Table 2 summarizes the boundary condition statement for each variable, on segments A-D of the boundary ∂R , see Figure 10a). Basically, line AB is a symmetry plane, CDA is the farfield potential boundary, and BC is inflow/outflow with vanishing normal derivatives.

The specification of suitable initial-conditions $\{QI(0)\}$ is a perplexing problem, since no experimental data are available for guidance. For the simu-lations reported, the initial jet was assumed to be either of circular or square cross-section, with a constant axial velocity (distribution) $\tilde{u}_1(x_1^0) \equiv U_j$. The initial $\tilde{u}_1$ distribution outside the initial jet cross-section was assumed constant at a level smaller than the initial jet velocity U_j. This constant was selected, dependent upon the particular test and the associated numerical stability. The constant is required non-zero, to prevent the 3DPNS equation set from becoming singular, dependent upon the imposed cross-flow velocity

23

D   C

A   a)   Transverse Solution Domain Discretization   B

U_∞

$|\leftarrow$ Jet $\longrightarrow|$

b)   Transverse Velocity Initialization $\tilde{u}_\ell(0)$
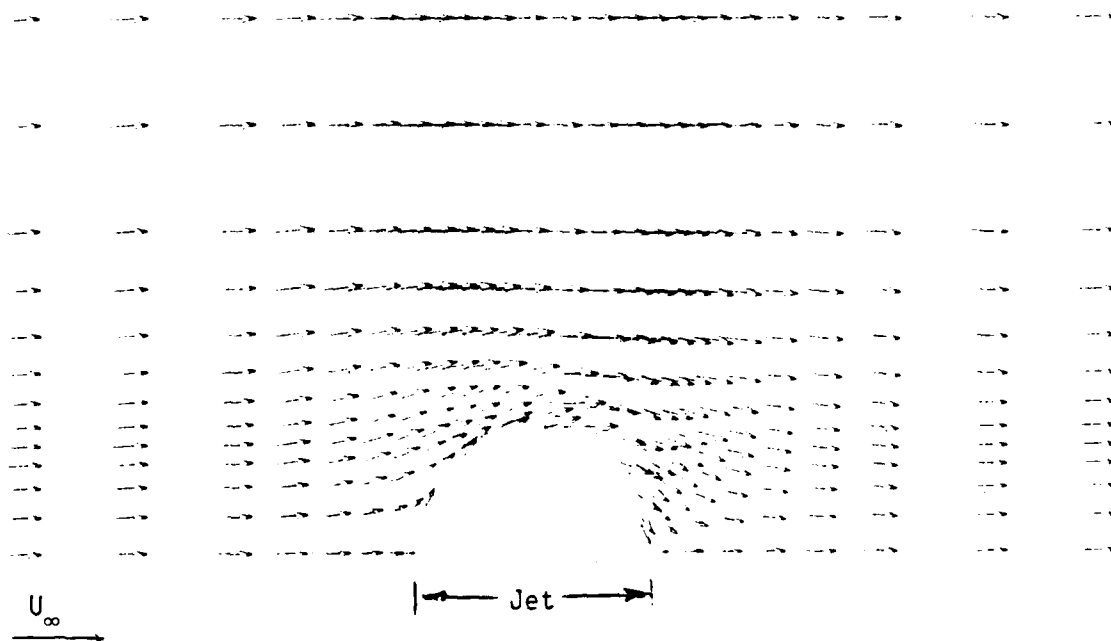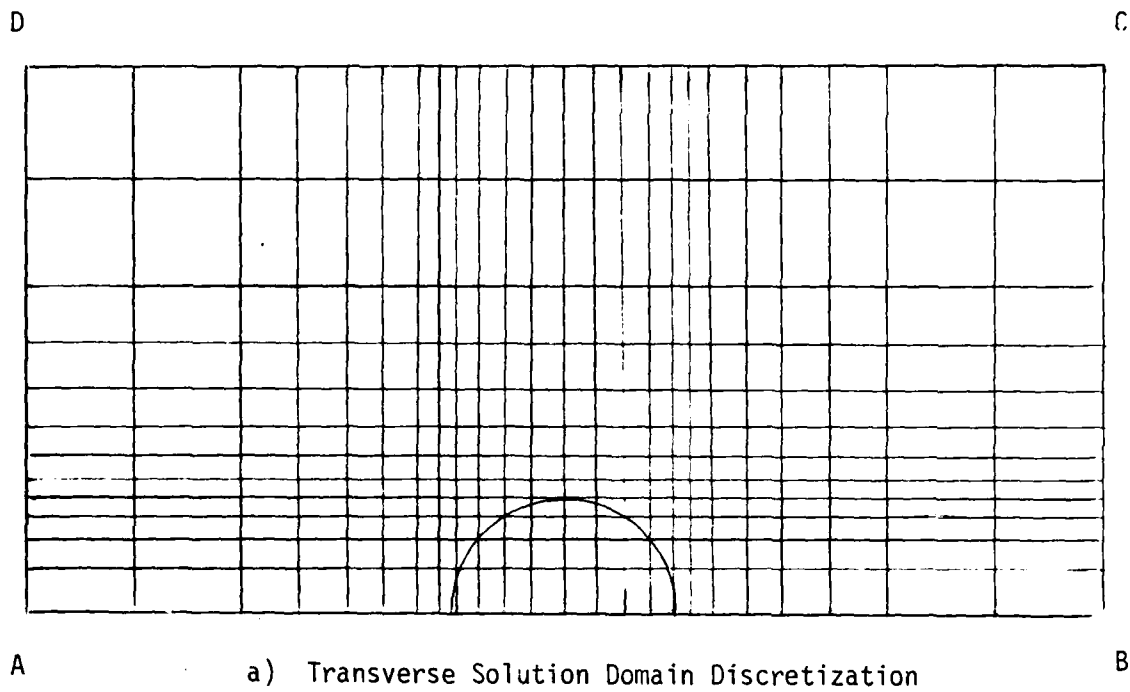
Figure 10   3DPNS Discretization Information For VSTOL Jet Simulation

Table 2

Boundary Condition Specifications for
3DPNS Simulation of VSTOL Jet in Cross-Flow

Variable	Equation	Boundary Segment	Boundary Condition
$\tilde{u}_1$	9	ABCDA	Zero normal derivative
$\tilde{u}_2$	30	AB	Zero
		BC	Vanishing normal derivative
		CDA	Specified cross-flow
$\tilde{u}_3$	30	ABC	Vanishing normal derivative
		CDA	Specified cross-flow
k	17	ABC	Vanishing normal derivative
		CDA	Fixed at freestream level
ϵ	18	ABC	Vanishing normal derivative
		CDA	Fixed at freestream level
P_c	12	ABC	Vanishing derivative
		CDA	Fixed at potential cross-flow
P_p	10	ABC	Vanishing derivative
		CDA	Zero
ϕ	31	AB	Vanishing derivative
		BCDA	Zero

level U_∞ (cf., the order of magnitude analysis). The VSTOL jet velocity ratio is thereby $\lambda = U_j/U_\infty$.

For tests conducted with zero cross-flow, the initial distribution for the transverse plane velocity field $\tilde{u}_\ell(x_i^\varrho, x_\ell)$ was zero. With $U_\infty > 0$, and following considerable numerical experimentation, the potential cylinder flow field shown in Figure 10b) was used to define $\tilde{u}_\ell(0)$ outside the initial jet. Inside the initial jet, $\tilde{u}_\ell(0) \equiv 0$. Thus, Bernoulli's equation yields the corresponding initial distribution of p_c on $\Omega(0)$.

Establishing suitable initial distributions for turbulent kinetic energy and dissipation function is more perplexing since the interaction on the up-stream face of the jet is extremely complicated. Since the project scope is to assess dominant factors, and in the total absence of data, a step distribution in turbulence levels was assumed appropriate. The initial level of turbulent kinetic energy k was assumed a distinct constant inside and outside the jet over $\Omega(0)$. The initial levels of dissipation were specified unique constants, as well, to produce distinct levels of turbulent kinematic viscosity $\nu^t \equiv C_4 k^2/\varepsilon$ inside and outside the jet, eg., $\nu_j^t \neq \nu_\infty^t$.

A series of computational experiments were required to ascertain numerically acceptable levels of k(0) and $\varepsilon(0)$, within the constraint $1 < \nu_j^t/\nu_\infty^t < 10^2$. The k and ε equations 17-18 are directly coupled in the non-homogeneous annihilation terms $\bar{\rho}\varepsilon$ and $\bar{\rho}\varepsilon^2/k$, and the farfield solutions depend strictly upon this balance (since all spatial gradients essentially vanish). Boundary levels for k and ε were fixed on segments CDA, Figure 10a), and the 3DPNS algorithm executed to determine solutions of equations 17-18 in the farfield. The new levels were then set on CDA, and the tests repeated until the interior solution and boundary data agreed. For $\nu_\infty^t \approx 10$, the suitable levels were determined as k(0) = 0.0005 and $\varepsilon(0)$ = 0.0012. For example, then for $\nu_j^t \approx 10^2$, k(0) = 0.005 and $\varepsilon(0)$ = 0.012 are acceptable initialization levels inside the jet.

Validation Numerical Results

As discussed in the following sub-section, the 3DPNS simulation of the VSTOL jet produces a transverse plane flowfield in substantial qualitative agreement with anticipated results and extensions of the modest data base. The requirement is to ascertain that the simulation is free from numerical disturbances that would by themselves produce such results. For this purpose,

26

several test cases were executed in the absence of an imposed crossflow, ie. $U_\infty \equiv 0$, to quantify algorithm performance with regards to symmetries and robust conservation of mass. The latter is particularly critical since the sole mechanism for generation of $\tilde{u}_\ell \neq 0$ is through continuity which is employed as the differential constraint on equation 30 that otherwise exhibits a null solution.

Examples were conducted for initially circular and/or square cross-section jets. Figure 11 shows the 3DPNS computed transverse velocity distributions on $0.5 \leq x_1/D \leq 2.0$, for a jet of initially square cross-section, for $U_\infty = 0$ and $U_j : U_j^- = 1.0 : 0.2$, where U_j is the $\tilde{u}_1(0)$ inside the jet and U_j^- is $\tilde{u}_1(0)$ outside the jet. The flow Reynolds number, based upon jet velocity (37 m/s) and jet diameter (width) is $Re = .6 \times 10^4$, and the turbulent kinematic viscosity $\nu^t \approx 10^2$ was held a constant. The computed velocity field exhibits essentially exact symmetry. Strong flow opposition is computed on the boundary of the jet at $x_1/D = 0.5$, and thereafter becomes more distributed throughout the initial "potential core." Note also the lateral spreading of the jet boundary, as defined by the opposing velocity vector locus. All velocity vector plots are scaled on the maximum scalar component of $\tilde{u}_\ell(x_1, x_\ell)$. The caption $\tilde{u}_\ell^m$ under each figure legend is the ratio of this maximum to U_j. Hence, note the extremum $\tilde{u}_\ell$ was reached at $x_1/D = 1.0$, $\tilde{u}_\ell^m = 0.026$, and thereafter decays by 30% in reaching $x_1/D = 2.0$.

Figure 12 shows the 3DPNS computed $\tilde{u}_\ell$ distributions on $0.5 \leq x_1/D \leq 1.0$, for the case in Figure 11 but with $U_j : U_j^- = 1.0 : 0.02$, ie., the farfield background for $\tilde{u}_1$ outside the jet is 1/50 of U_j. Comparing to Figure 11, a significantly stronger entrainment field is induced at $x_1/D = 0.5$ ($\tilde{u}_\ell^m = 0.086$), but thereafter there is no consequential difference. This test addresses the issue of the 3DPNS order of magnitude analysis, wherein $0(\delta) < 0(1)$ by some unspecified amount. For the test of Figure 11, $0(\delta) = 0(u_j/\tilde{u}_\ell^m)^{-1} \approx 0(10^{-1})$, while for Figure 12, $0(\delta) = 0(0.02/0.05)^{-1} \approx 0(1)$. For the cases with non-zero crossflow, where $U_j : U_\infty = 1.0 : 0.1$, these results indicate that for the farfield level of $U_j^- \approx U_\infty$, the 3DPNS algorithm should function, although in this region $0(\delta) \approx 0(1)$ is not robust adherence to the ordering analysis. Some detailed solution differences would occur for U_j^- not a uniform constant; the evolution of $\tilde{u}_\ell(x_1)$ would remain essentially unchanged, however, based upon these results.

The final validation is quantization of the algorithm capability to predict turbulent shear layer interaction on a grid discretization as coarse as shown in Figure 10a). For this purpose, the two-dimensional algorithm (2DPNS) was

27
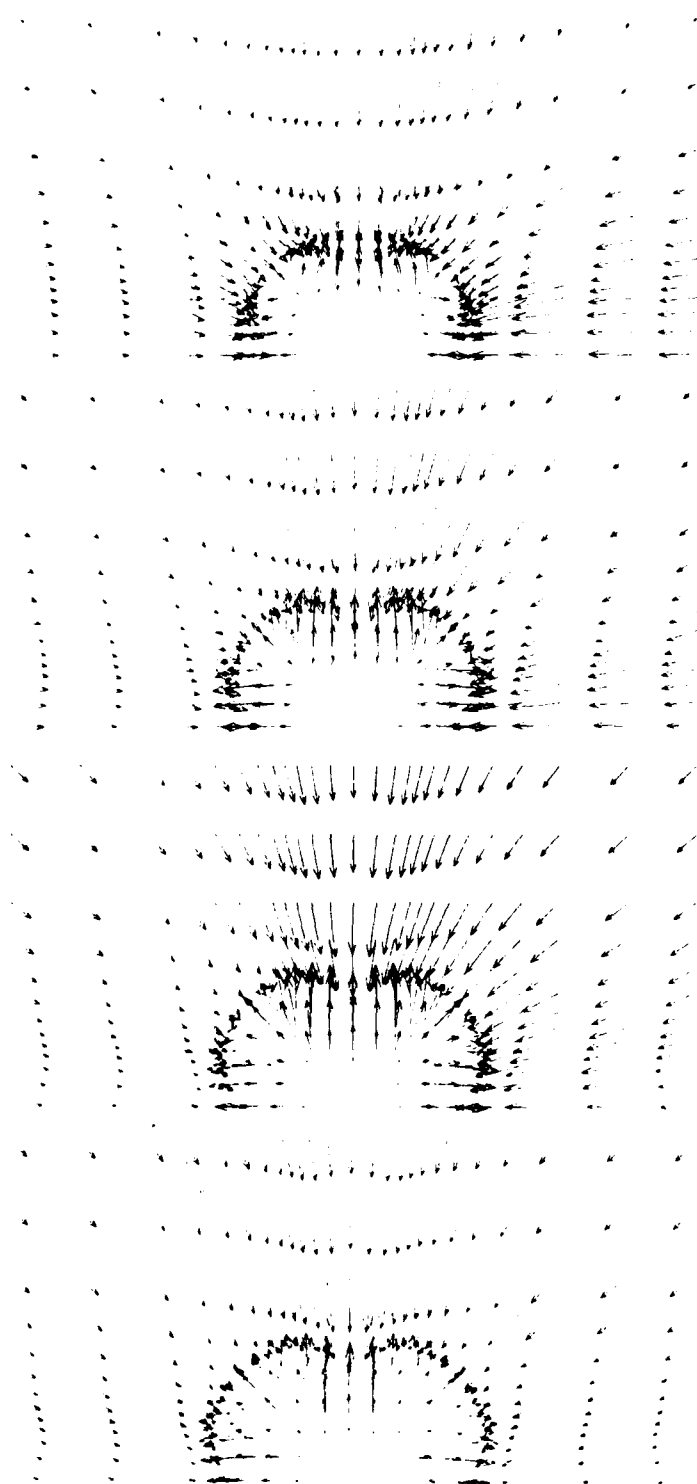
a) $x_1/D = 0.5$

$\tilde{u}^m_\ell = 0.013$

b) $x_1/D = 1.0$

$u^m_\ell = 0.026$

c) $x_1/D = 1.5$

$\tilde{u}^m_\ell = 0.021$

d) $x_1/D = 2.0$

$\tilde{u}^m_\ell = 0.017$

Figure 11.   3DPNS Computed Transverse Plane Velocity Vector Distributions, Square Jet, $U_j/U^-_j/U_\infty = 1.0/0.2/0.0$, $\nu^t = 10^2$.
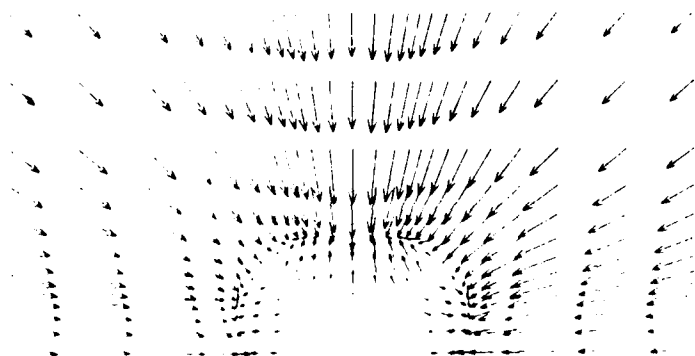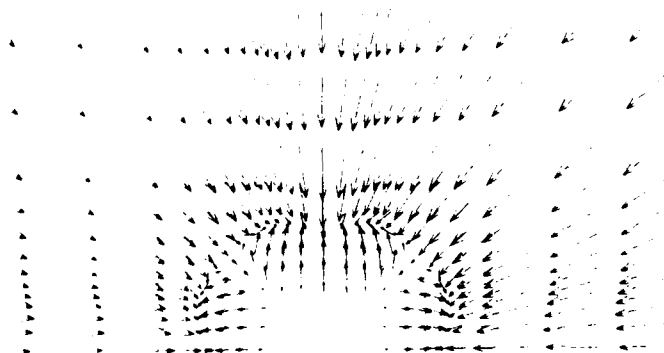
a) $x_1/D = 0.5$

$\tilde{u}_\ell^m = 0.086$

b) $x_1/D = 1.0$

$\tilde{u}_\ell^m = 0.052$

Figure 12.   3DPNS Computed Transverse Plane Velocity Vector Distributions Square Jet, $U_j/U_j^-/U_\infty = 1.0/0.02/0.0$, $\nu^t = 10^2$.

29

executed to simulate a turbulent slot jet flow at $U_j:U_j^- = 1.0:0.02$, using a uniform discretization of R^1 of mesh measure equal to that for the smallest element domains shown in Figure 10a), as located on the boundary of the jet. Figure 13 summarizes the 2DPNS solution on $0 \leq x_1/D \leq 1.0$, for a unit Reynolds number/Length of $Re = 0.2 \times 10^7/m$. The action of turbulent viscosity smoothly erodes the slot jet boundary. Entrainment from the farfield, $\tilde{u}_2 < 0$, and definition of the jet boundary by the sign change in $\tilde{u}_2$, is clearly illustrated in Figure 13b). The initial distributions $k(0)$ and $\epsilon(0)$ were determined from elementary mixing length theory [16]. The solutions for k and ϵ, Figures 13c)-d) show the rapid growth in both variables at the edge of the slot jet. The resulting decay of these peak levels, as the strain rate $\partial \tilde{u}_1/\partial x_2$ diminishes (hence also the non-homogeneous source term in the k and ϵ equations 17-18), is also evident.

Figure 14 shows the corresponding computed distributions of the Reynolds stress tensor, equations 13-16. The axial normal stress $\overline{u_1'u_1'}$ exhibits larger gradients and peak levels, in comparison to the transverse normal stress $\overline{u_2'u_2'}$, due both to the difference between C_1 and C_3, and the action of the $O(\delta^2)$ term. This latter influence is documented [20] of dominant importance in promoting prediction agreement with detailed experimental data for an airfoil trailing edge wake flow. The Reynolds shear stress and turbulent kinematic viscosity distributions exhibit similar trends.

Circular VSTOL Jet Simulation Results

The principal subject is analysis of a circular cross-section, subsonic VSTOL jet, issued perpendicular to a flat plate into a subsonic crossflow at velocity ratio $\lambda = U_j/U_\infty = 10$. The results of the validation test cases, and additional numerical experiments, provided the initialization procedure. The initial plateau distributions of axial velocity $\tilde{u}_1(0)$ and the reference cross-flow, were set at $U_j:U_j^-:U_\infty = 1.0:0.2:0.1$, with $U_j = 36.6$ m/s (120f/s). In the absence of better guidance, the initial velocity U_j^- exterior to the jet was assumed a uniform constant, to preclude occurrence of fictitious farfield gradients. The initial distribution for transverse velocity $\tilde{u}_\ell(0)$ is potential flow about a cylinder, Figure 10b). The initial levels for turbulence kinetic energy $k(0) \geq 0.0005$ and dissipation $\epsilon(0) \leq 0.0012$ were set at distinct constant levels inside/outside the initial jet to produce the desired initial levels of $1 < \nu^t < 100$. The reference Reynolds number based on jet orifice diameter is $Re = 0.6 \times 10^4$.
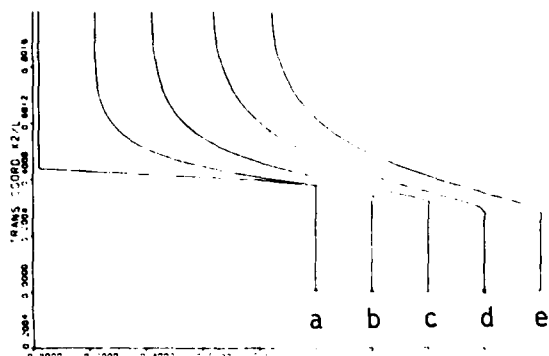
a) Axial Velocity $\tilde{u}_1$
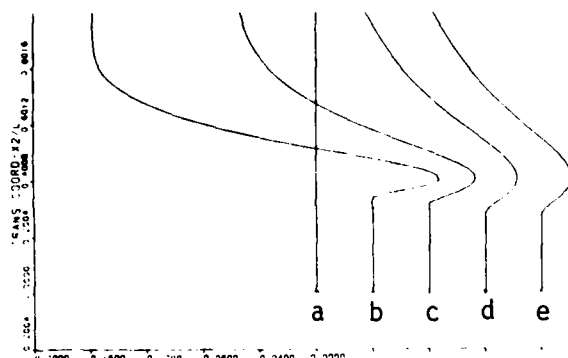
b) Transverse Velocity $\tilde{u}_2$
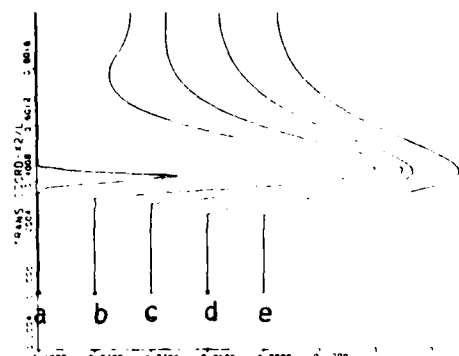
c) Turbulent Kinetic Energy k
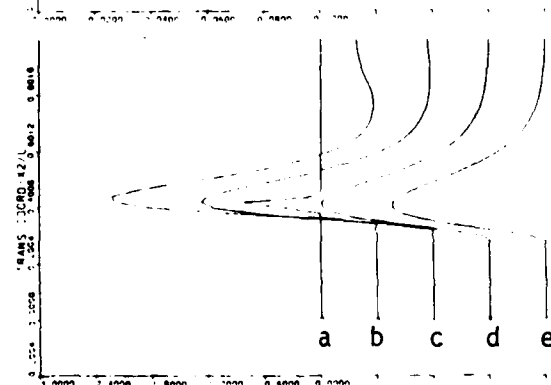
d) Dissipation Function ϵ

Figure 13.   2DPNS Computed Solution Field, Turbulent Rectangular
                Slot Jet Flow, $U_j/U_j^- = 1.0/0.02$, $x_1/D = \{0, .25, .5, .75, 1.0\}$ =
                                                                $\{a, b, c, d, e\}$.

31
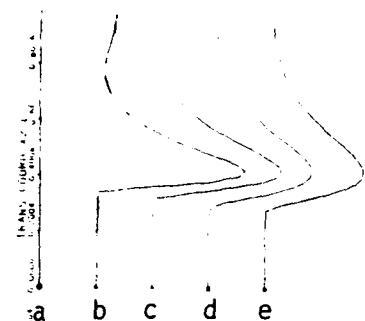
a) Normal Stress $\overline{u_1 u_1}$
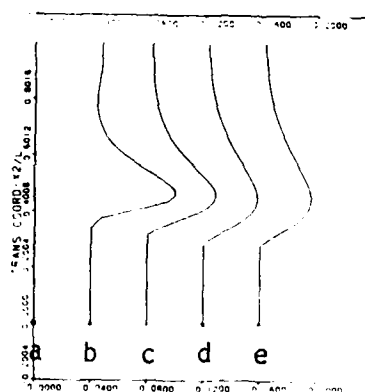
b) Normal Stress $\overline{u_2 u_2}$
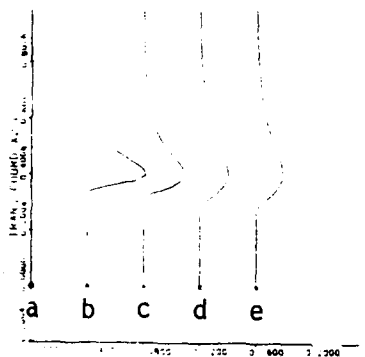
c) Shear Stress $\overline{u_1 u_2}$
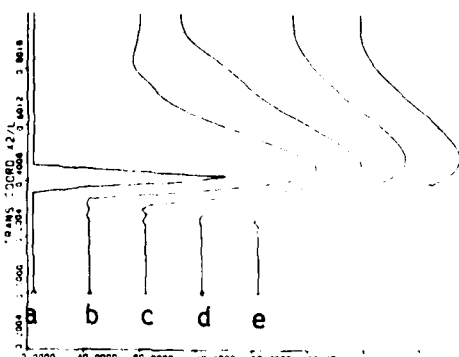
d) Turbulent Viscosity ν^t

Figure 14.   2DPNS Computed Reynolds Stress Distributions,
            Turbulent Rectangular Slot Jet Flow, x_1/D = {0, .25, .5, .75, 1.0} =

{a, b, c, d, e}.

The necessary comparison results were for this specification in the absence of cross-flow, ie., U_∞ = 0. Figure 15 summarizes the 3DPNS solution for transverse velocity distributions on $0.25 \leq x_1/D \leq 1.25$ for laminar flow. Figure 16 shows the comparison turbulent flow results for $v^t(0) \approx 10^2$ inside the jet and $v^t(0) \sim 10$ everywhere exterior to the jet. Both figures illustrate the continuity-induced generation and entrainment of a farfield transverse velocity distribution. The extremum velocity magnitude occurs on the jet boundary for both cases; however, the laminar farfield magnitude is considerably smaller, in comparison to its extremum, than for the turbulent case, see Figures 15c) and 16c). Of greater fluid dynamic significance regarding entrainment, the extremum turbulent transverse velocities are a factor of 20 or more larger than the laminar flow extrema. This ratio is a quantitative indicator of the enhanced entrainment efficiency of the turbulent jet. Figure 17 shows the 3DPNS solution distributions for q_i^h = {$\tilde{u}_1$, k, ε} at x_1/D = 1.25, for the turbulent circular jet in zero cross-flow. The contour levels are labeled and shown in the appropriate legend. The distributions for $\tilde{u}_1$ and k are close approximations to axisymmetric, with a slight flattening indicated along the 45° and 135° rays from the center. This is a grid induced effect, primarily the consequence of the initial condition approximation on the union of rectangles, Figure 10a). This can be observed in the smallest contour level for ε = 0.020, Figure 17c), which lies just above the background initialization level of $\varepsilon(0)$ = 0.012. Since the application of $U_\infty \neq 0$ will destroy any point symmetry anyway, these results are taken as confirmation that the selected combination of discretization, boundary constraints and initial conditions for the 3DPNS VSTOL jet simulation will not induce a spurious flowfield skewing of measurable consequence.

Figure 18 shows the 3DPNS algorithm computed evolution of the transverse velocity field on $0 < x_1/D \leq 1.25$, for the circular, turbulent VSTOL jet in a cross-flow, $U_j : U_j^- : U_\infty$ = 1.0:0.2:0.1. The extremum transverse scalar component, upon which each figure is scaled is noted in each legend. The blockage effect of the jet is immediately evident, Figure 18b), as is the beginning of entrainment in the lateral farfield. The transverse velocity field begins to penetrate the downstream interface of the jet by x_1/D = 0.5, Figure 18c), and a decrease in the outflow in the wake region is evident. This becomes considerably pronounced by x_1/D = 0.75, Figure 18d), where wake flow reversal has begun.
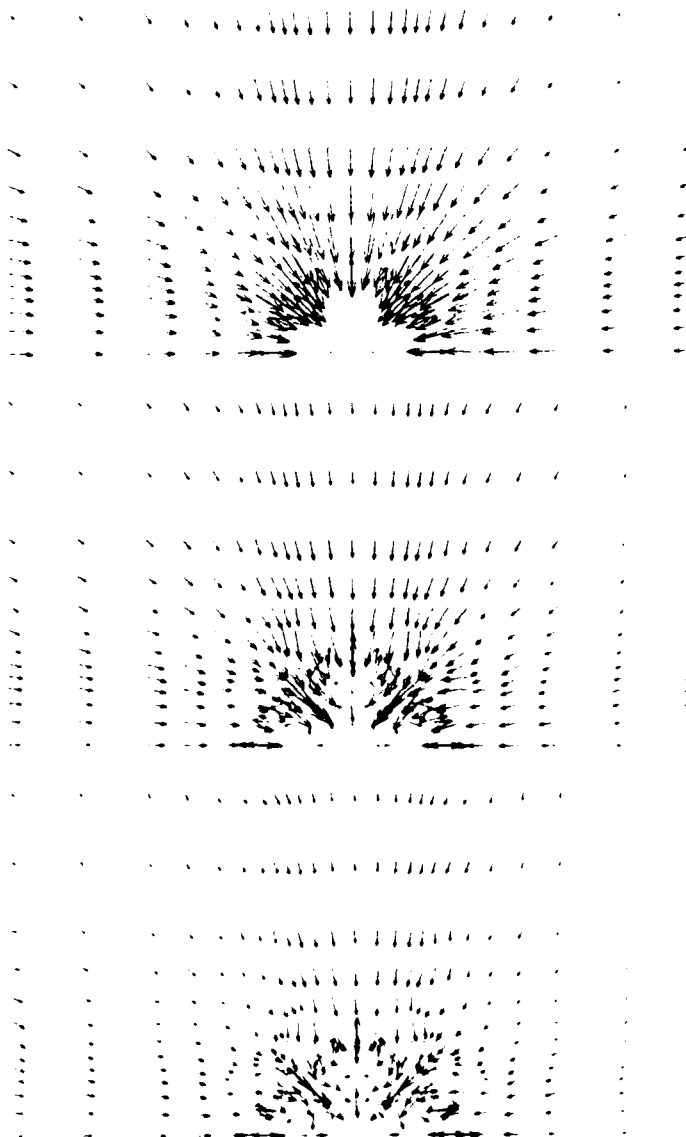
a) $x_1/D = 0.25$

$u_\ell^m = 0.0015$

b) $x_1/D = 0.75$

$u_\ell^m = 0.0015$

c) $x_1/D = 1.25$

$u_\ell^m = 0.0018$

Figure 15.   3DPNS Computed Transverse Velocity Distributions,
Laminar Circular Jet, Zero Cross-Flow.

a) $x_1/D = 0.25$

$\tilde{u}_\ell^m = 0.039$

b) $x_1/D = 0.75$

$\tilde{u}_\ell^m = 0.052$

c) $x_1/D = 1.25$

$\tilde{u}_\ell^m = 0.034$
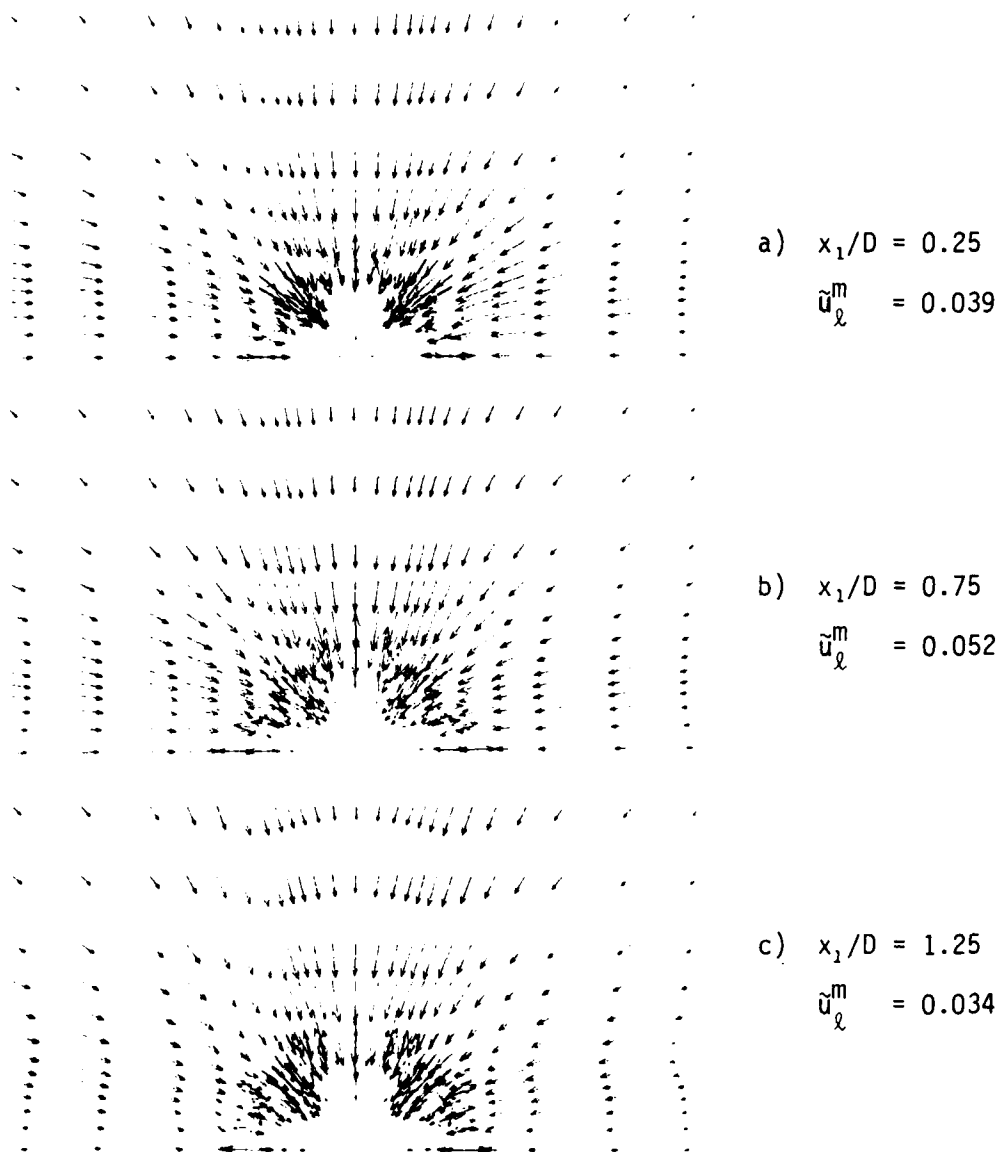
Figure 16.   3DPNS Computed Transverse Velocity Distributions,
Turbulent Circular Jet, Zero Cross-Flow.

35

a) Axial Velocity $\tilde{u}_1$

$\{a, b, d, d, e\} =$
$\{.3, .5, .7, .9, 1.0\}$

e d c b a

b) Turbulent Energy k

$\{a, b, c, d\} =$
$\{.013, .025, .040, .044\}$

$^a{}_b{}^c{}_d{}^c{}_b{}^a$

c) Dissipation Function ε

$\{a, b, c, d\} =$
$\{.02, .2, .5, .65\}$

$^a{}_b{}^c{}_{\mathbf{d}}{}^{\mathbf{c}}\ _b{}^a$

Figure 17.   3DPNS Computed Solution {QI},
        Turbulent Circular Jet, Zero Cross-Flow, $x_1/D = 1.25$

a) $x_1/D = 0.0$

$\tilde{u}_\ell^m = 0.174$

b) $x_1/D = 0.25$

$\tilde{u}_\ell^m = 0.176$

c) $x_1/D = 0.50$

$\tilde{u}_\ell^m = 0.160$
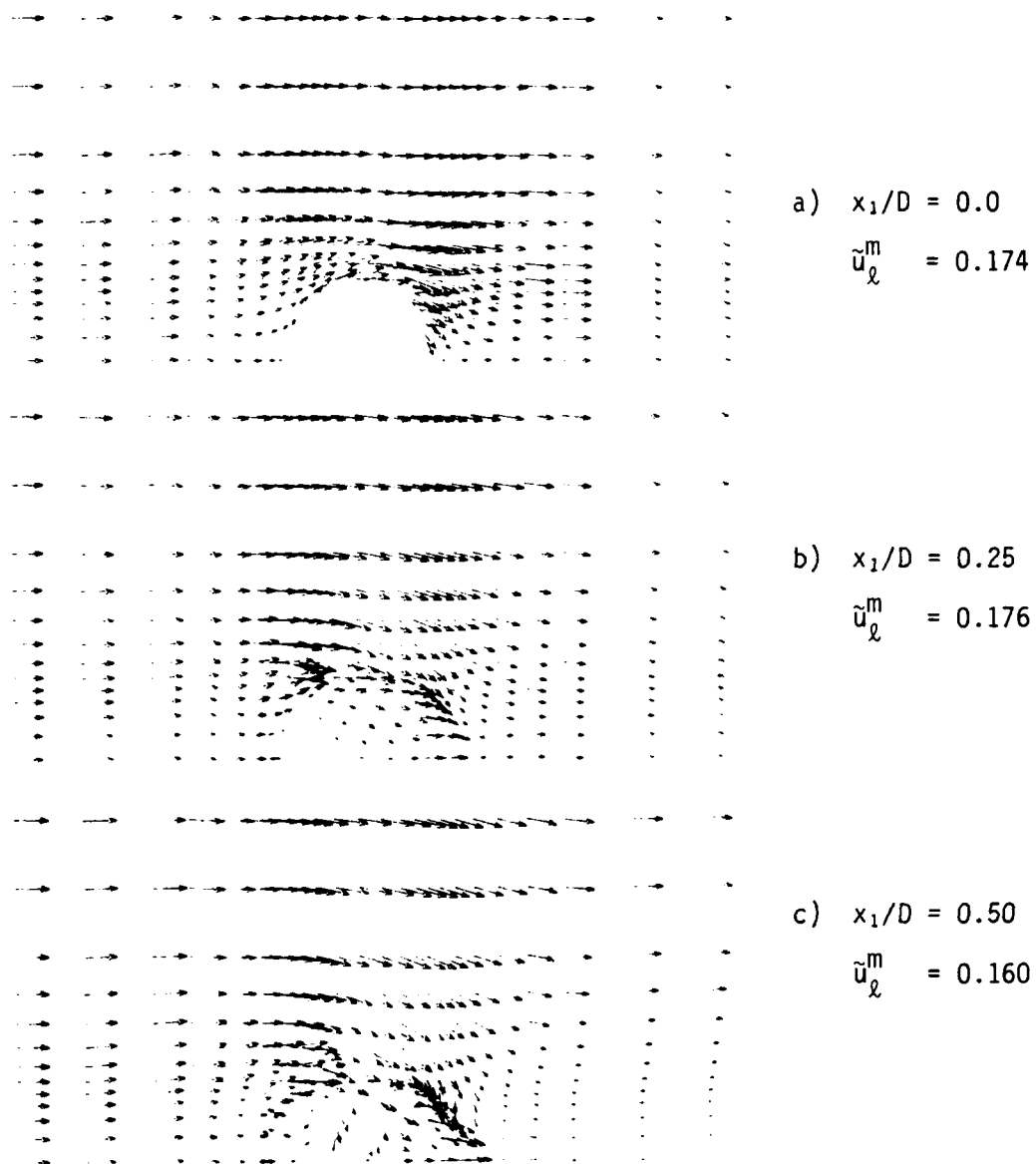
Figure 18   3DPNS Computed Transverse Velocity Distributions,
Circular VSTOL Jet, $U_j/U_j^-/U_\infty$ = 1.0/0.2/0.1, Turbulent
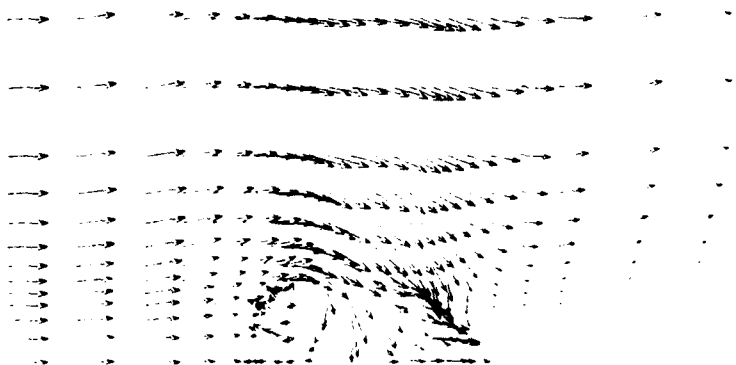
d) $x_1/D = 0.75$

$\tilde{u}_\ell^m = 0.136$

e) $x_1/D = 1.0$

$\tilde{u}_\ell^m = 0.110$

f) $x_1/D = 1.25$

$\tilde{u}_\ell^m = 0.102$

Figure 18 cont. 3DPNS Computed Transverse Velocity Distributions, Circular VSTOL Jet, $U_j U_j^-/U_\infty = 1.0/0.2/0.1$, Turbulent

The entrainment from the lateral farfield has also become stronger with penetration on the lee side of the jet. The vortex structure interior to the initial jet becomes fully developed by $x_1/D = 1.0$, Figure 18e). The combined actions of blockage, entrainment, wake flow reversal and axial vortex are each matured and clearly evident in the solution at $x_1/D = 1.25$, Figure 18f).

The results of Figure 18 can be interpreted as a consequential indication that the 3DPNS simulation procedure exhibits potential for prediction of the near-field essential characteristic action of the elementary VSTOL jet in cross-flow. In particular, the region of reversed flow and angle of the wake streamline, Figure 18f), are in qualitative agreement with the oilflow streakline experiment results, Figures 1-2. The generation of the axial vortex (pair) is in qualitative agreement with farfield data [10-12] see Figure 4. The jet boundary is not impervious to the cross-flow and the intrusion of entrainment is predicted on the downstream face of the jet. However, as clearly emphasized in the preceeding discussions, these results are consequentially influenced by the many decisions and compromises required to complete the mathematical specification, in particular the initial conditions and size and refinement of the computational solution domain. These are detailed aspects that require individual attention. The impetus to attack these subjects is hopefully enhanced by the encourageing results of this prediction.

Additional computational tests were conducted to quantize the influence of gross turbulence factor modifications. Figure 19 summarizes the results for the VSTOL jet specification of Figure 18. Figures 19a)-b) show the transverse velocity field $\tilde{u}_\ell$ on $0.5 \leq x_1/D \leq 1.0$ computed holding $\nu^t \equiv 10$, a constant throughout the entire solution domain. Some farfield entrainment action occurs, but the nearfield crossflow appears almost negligibly deflected. Figure 19c) shows the comparison solution at $x_1/D = 0.5$, for constant ν^t but with $\nu_j^t \equiv 100$. The jet is considerably more impervious to the crossflow. In comparison to Figure 18c), a somewhat greater deflection of the upstream farfield has occurred, and downstream penetration is essentially absent. For the variable turbulence simulation, Figure 18, an extremum $\nu^t \approx 160$ was computed on the jet boundary at $x_1/D = 0.5$. Clearly, the turbulence phenomena exerts a predominant influence on predicted results which adds further emphasis to the need to obtain appropriate high quality experimental data.

a) $x_2/D = 0.5$

$\nu^t = 10/10$

$\tilde{u}_\ell^m = 0.107$

b) $x_1/D = 1.0$

$\nu^t = 10/10$

$\tilde{u}_\ell^m = 0.109$

c) $x_1/D = 0.5$

$\nu^t = 100/10$

$\tilde{u}_\ell^m = 0.139$
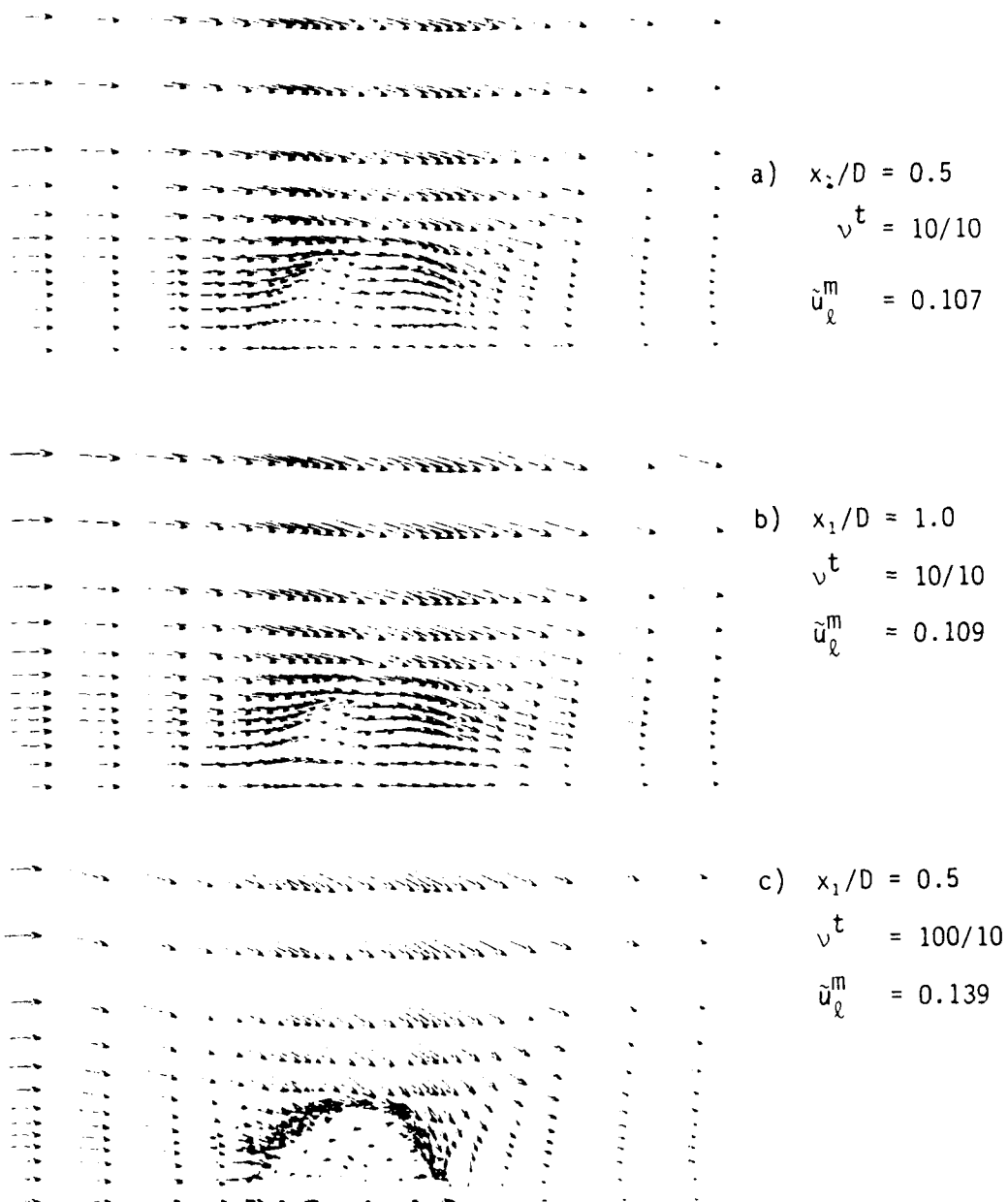
Figure 19   3DPNS Assessment Of Gross Turbulence Modifications,
              Circular VSTOL Jet, $U_j U_j^-/U_\infty = 1.0/0.2/0.1$

Figure 20 shows the 3DPNS solution distributions for $q_i^h = \{\tilde{u}_1, k, \epsilon\}$ at $x_1/D = 1.25$, for the turbulent circular jet with cross-flow, $U_j:U_j^-:U_\infty = 1.0:$ 0.2:0.1. (The transverse velocity solutions are shown in Figure 18.) The contour levels are labeled and numbered in the appropriate legend. The exact comparison solution for zero cross-flow is shown in Figure 17, and distinct differences are noted. In general, the essential axisymmetry for zero cross-flow has been altered, with cross-flow applied, and for $x_1/D = 1.25$, the profile transverse spans are quite flattened with the isoclines somewhat distended upstream along a nominal 135^0 ray from the circle center. The extremum level contours for k and ϵ both occupy a larger region of R^2, generally within the interval $135^0 \leq \alpha \leq 180^0$. These results appear the combined influence of the lateral constraint influence of cross-flow, counter-balanced with the effects of entrainment and core vortex convection to distend the flow profiles preferentially in the upstream quadrant.
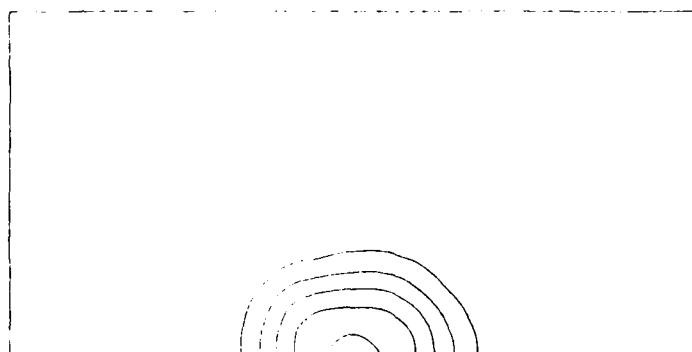
a) Axial Velocity $\bar{u}_1$
$\{a, b, c, d, e\} =$
$\{.3, .5, .7, .9, 1.0\}$
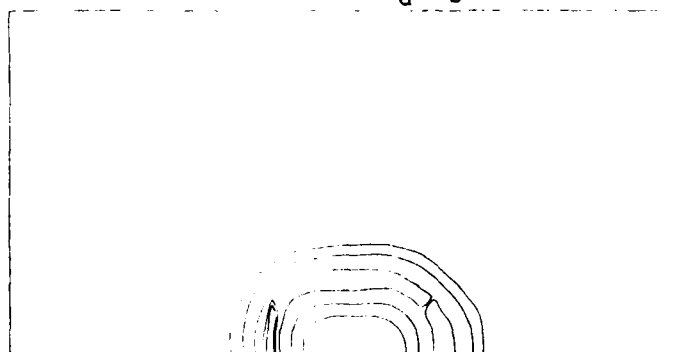
b) Turbulent Energy k
$\{a, b, c, d\} =$
$\{.013, .025, .040, .045\}$
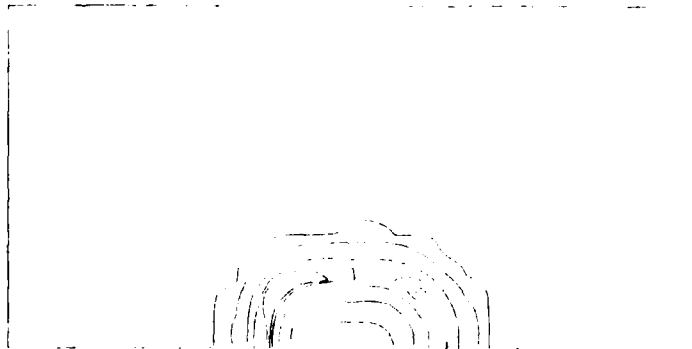
c) Dissipation Function ϵ
$\{a, b, c, d, e\}$
$\{.02, .2, .5, .65, .7\}$

Figure 20.   3DPNS Computed Solution {QI}
Turbulent Circular Jet With Cross Flow, $\lambda = 10$,
$x_1/D = 1.25$.

42

SUMMARY AND CONCLUSIONS

A mathematical model has been constructed for analysis of the near-field evolution of the basic VSTOL jet in an applied subsonic crossflow. The resultant numerical approximation has utilized a continuity-constrained, finite element algorithm for solution of the parabolized form of the time-averaged, steady three-dimensional Navier-Stokes equations for turbulent flow. A Reynolds stress constitutive equation was employed for turbulence closure which required numerical solution of the parabolized three-dimensional form of the turbulent kinetic energy and dissipation function transport equations. Various documentory tests were executed to validate correct operation of the COMOC:3DPNS computer program embodiment of the theory.

The results of the computational simulations of the VSTOL jet, with and without application of a subsonic crossflow, have yielded results of technical interest and anticipated merit. Of greatest significance, the constructed 3DPNS model, when operated without fictitious constraints on the turbulence field (evolution), produced a flowfield solution for the circular jet in substantial qualitative agreement with the available sparse data. Without initial-condition generated bias, and using the most elementary solution starting conditions, the 3DPNS model predicted the essential evolution character in substantial completeness. In particular, the simulation predicted lateral entrainment, axial vortex-pair initiation and inducement of the wake flow into the jet region, antiparallel to the initialized potential crossflow direction. These documented features of the VSTOL jet were generally lost when the turbulence field was artificially constrained, indicating that the characteristic action is a turbulence-dominated effect.

It should be emphasized as well that none of the flow characteristics were consequentially captured without robust enforcement of the (non-parabolic) continuity equation. The developed constraint algorithm met the detailed mathematical requirements and accurately enforced the detailed solution aspects related to the 3DPNS ordering analysis. In particular, the finite element based algorithm maintained the (energy norm) error in exact satisfaction of continuity at $E(.,.) \leq 6. \times 10^{-5}$ for algorithm convergence set at $\epsilon = 10^{-4}$. The 3DPNS algorithm averaged four iterations per step for convergence following a few extra iterations to homogenize initial condition error. The solution on $0 \leq x_1/D < 1.25$ required approximately 60 CPU minutes to execute on a CYBER 175

43

computer, using 200K single precision words of central memory.

These results are interpreted as highly encouraging with respect to constituting a basic proof of concept. Clearly, the utilized discretization is too coarse by an order of magnitude, and the transverse domain span too small by a factor of two or more. The total absence of any data to help generate initial condition distributions is certainly a liability. Nevertheless, the numerical simulation capability is three-dimensional and turbulent, and has provided some valuable and interesting insight to quantify dominant aspects. The discretization and domain span constraints are strictly computer details (that can be solved by utilizing the CYBER 20X, for example). The 3DPNS algorithm can be directly extended to compressible and non-isoenergetic flows, hence be rendered applicable to the more practical problem involving heated jets (exhaust). The Reynolds stress closure model could be replaced by solution of the parabolized Reynolds stress transport equations, or even more elegant procedures, if and when it is deemed necessary and/or appropriate. Each of these issues constitutes a particular detail, building upon the basic structure of the computational model and computer program. The 3DPNS model could be of considerable usefulness, for engineering analysis, pending emergence of the complete 3DNS numerical solution capability (and the CYBER 20X^2 or NASF).

REFERENCES

1. Chang, H. C., "The Roll-Up Of A Cylindrical Jet In A Cross-Flow," Aerospace Research Laboratories Report ARL 73-0131, 1973.

2. Wooler, P. T., "Development Of An Analytical Model For The Flow Of A Jet Into A Subsonic Cross-Wind," NASA SP-218, p. 101-118, 1968.

3. Schmidt, H., "Deflection Of A Round Turbulent Jet In A Cross-Wind," Arch. Mech., Vol. 26, Pt. 5, p. 849-859, 1974.

4. Jordinson, R., "Flow In A Jet Directed Normal To The Wind," ARC Report And Memoranda No. 3074, 1956.

5. Moussa, A. F., Trischka, J. W. And Eskinazi, F., "The Near Field In The Mixing Of A Round Jet With A Cross-Stream," J. Flu. Mech., Vol. 80, Pt. 1, p. 49-80, 1977.

6. Vogler, R. D., "Surface Pressure Distributions Induced On A Flat Plate By A Cold Air Jet Issuing Perpendicularly From The Plate And Normal To A Low-Speed Free Stream Flow," NASA TN D-1629, 1963.

7. Bradbury, L. J. S., And Wood, M. N., "The Static Pressure Distribution Around A Circular Jet Exhausting Normally From A Plane Wall Into An Airstream," C. P. No. 822, 1965, British Aero. Res. Council.

8. McMahon, H. M. and Mosher, D. K., "Experimental Investigation Of Pressures Induced On A Flat Plate By A Jet Issuing Into A Subsonic Crosswind," NASA SP-218, p. 49-62, 1968.

9. Margason, R. J. and Fearn, R., "Jet-Wake Characteristics And Their Induced Aerodynamic Effects On V/STOL Aircraft In Transition Flight," NASA SP-218, p. 1-18, 1968.

10. Mosher, D. K., "An Experimental Investigation Of A Turbulent Jet In A Cross-Flow," Aerospace Engineering Report No. 70-7, Georgia Institute Of Technology, 1970.

11. Kamotani, Y. And Greber, I., "Experiments On A Turbulent Jet In A Cross-Flow," AIAA J., Vol, 10, No. 11, p. 1425-29, 1972.

12. Fearn, R. & Weston, R. P., "Vorticity Associated With A Jet In A Cross-Flow," AIAA J., Vol. 12, No. 12, p. 1666-1671, 1974.

13. Fearn, R. L. and Weston, R. P., "Induced Pressure Distributions Of A Jet In A Cross-Flow," NASA TN-D-7916, 1976.

14. Thames, F. C. And Weston, R. P., "Properties Of Aspect-Ratio 4.0 Rectangular Jets In A Subsonic Cross-Flow," AIAA Paper No. 78-1508, 1978.

15. Baker, A. J., Manhardt, P. D., and Yen, K. T., "A Numerical Interaction Algorithm For Prediction of VSTOL Jet-Induced Flowfields," Proceedings, V/STOL Aircraft Aerodynamics, Vol. 1, pp. 204-227, 1979.

16. Cebeci, T. and Smith, A.M.O. Analysis of Turbulent Boundary Layers, Academic Press, New York, 1974.

17. Launder, B.E., Reece, G.J. and Rodi, W., "Progress in the Development of a Reynolds-Stress Turbulence Closure," J. Flu. Mech., V. 68, Pt. 3, pp. 537-566, 1975.

18. Hanjalic, K. and Launder, B.E., "A Reynolds Stress Model of Turbulence and its Application to Thin Shear Flows," J. Flu. Mech., V. 52, Pt. 4, pp. 609-638, 1972.

19. Baker, A.J. and Orzechowski, J.A., "A Continuity Constraint Finite Element Algorithm for Three-Dimensional Parabolic Flow Prediction," Technical Paper to be presented at ASME Winter Annual Meeting, Washington, DC, Nov. 1981.

20. Baker, A.J., Yu, J.C., Orzechowski, J.A., and Gatsi, T.B., "Prediction and Measurement of Turbulent Aerodynamic Trailing Edge Flows," AIAA Paper No. 80-1395, 1980.

21. Gessner, F.B. and Emery, A.F., "A Reynolds Stress Model for Turbulent Corner Flows - Pt. I: Development of the Model," J. Flu. Engr., Trans. ASME, pp. 261-268, 1976.

22. Baker, A.J., Finite Element Computational Fluid Mechanics, McGraw-Hill/ Hemisphere, N.Y., 1982 (Tentative).

23. Manhardt, P.D. and Orzechowski, J.A., "COMOC:3DPNS Computer Program User's Manual," Final Report for NASA Contract NAS1-15105, 1982.

24. Melling, A. and Whitelaw, J.H., "Turbulent Flow in a Rectangular Duct," J. Fluid Mech., V. 78, Pt. 2, pp. 289-315, 1976.

APPENDIX

DATA DECK SPECIFICATIONS

Input facilities for the COMOC IV Parabolic Navier Stokes computer program are sophisticated and greatly simplify data deck preparation and modification. The program sequentially scans the data deck and operates on command data cards as they are encountered. Numerical data required for each command operation are input in free format on cards directly following the command card. Command operations can cause arrays to be filled, initiate a series of solution operations or specify output formats and titles. Command card sequence is quite flexible and care has been taken to ensure that most operations which must be performed sequentially are specifiable under one command name.

Most numerical data may be input in free format. Data delimiters may be blanks or commas, thus allowing for esthetic and meaningful arrangement of data and simple addition or deletion of interspersed numbers. Several features of free format input which greatly simplify repetitive and sequential data specifications are:

<u>Repetitive Numbers</u>:	12.5*7
Fills Array	12. 7. 7. 7. 7. 7.
<u>Repetitive Sequence</u> (One per card only)	2(5. 2. 4.
Fills Array	5. 2. 4. 5. 2. 4.
<u>Skip P locations</u>	10. 12. 3*P 22. T
Fills Array	10. 12. ∇ ∇ ∇ 22.
<u>Increment by a constant</u>	5*50 10 T
Fills Array	10 60 110 160 210
<u>Exponential Notation</u>	6. 10.0E-2 14.0E-4 T
Fills Array	6. 0.1.0014

The data deck for a VSTOL jet in a crossflow solution is segmented into several sections for description, but appears in sequential order as indicated by line numbers. The data has been lumped into meaningful categories, each of which can be related to specific differential equation solution components. (e.g., initial condtions, boundary conditions, etc.). The Fortran MAIN program contains global dimensioning and initialization of the primary differential equation coefficient arrays and parameter lists. A listing of MAIN together with subroutines GETTPR and NODPPR, which provide flow initial conditions specific to the jet crossflow problem, follow the data deck description.

I. NAMELIST (Integer Scalar) Input

```
2 3DPNS
3 FEBNAME                T READ NAMELIST PARAMETER DATA - INTEGER,REAL
4 &NAME01
5       NODE = 330,    LCOL = 30,      KROW = 30,
6       NM = 3,        NDP = 10,
7       NEQ = 9,       NEQKNN = 5,     NEQADD = -4,
8       NEQAV2 = 1,    NEQAV3 = 1,     NCNADD = 5,
9       NPVSX = 30,    NTABPI = 3,     ITKE = 1,
10      IBLAS = 2,     IUONLY = 3,
11      NIMPLT = 1,    NBAND = 29,     NCNTIT = 0,
12      KNTPAS = 4,    NPRNT = 132,    NTPRNT = 99999,    NC = 8,
13 &END
```

Line	Command	
2	3DPNS	Solution procedure (3D Parabolic Navier-Stokes)
3	FEBANE	Command to initiate Namelist read
4	&NAME01	Integar Namelist Data
5	NODE	Slightly larger than the number of nodes in the solution
	LCOL	Larger than the number of nodes along abcissa
	KROW	Larger than the number of nodes along the ordinate
6	NDP	No. of Differential Equations plus No. of parameter arrays required
7	NEQ	No. of Dependent Variables
	NEQKNN	No. of Differential Equations solved
	NEQADD	No. of Differential Equations initially not solved
8	NEQAV2,3	Set to 1 to integrate variables U_2 and U_3
	NCNADD	Begin U_2, U_3 integration after NCNADD steps
9	NPVSX	Number of points in the input Pc Table
	ITKE	Flag indicating solution of the turbulent shear stresses
10	IBLAS	U_2, U_3 convergence multipliers in EPS
	IUONLY	Number of steps until convergence on U1 only
11	NIMPLT	Use implicit Newton Iteration procedure
	NBAND	Maximum bandwidth of Jacobian Matrix
	NCNTIT	Pass counter to start perturbation pressure solution
12	KNTPASS	Maximum number of integration steps between prints
	NPRNT	Number of columns on a line of output
	NTPRNT	Exclude integral parameter print
	NC	Output format number field width
13	&END	End of Integer Namelist Data

II. NAMELIST (Real-Scalar) Input

```
14 &NAME02
15     UINF = 120.,    TOFINF = 533.,   REFL = .0328084,
16     GUMULT = 1.,
17     OSG = 1.,       PPFACT = 1.,     PCFACT = 1.,
18     VLDMLT = 1.,    VCMULT = 1.,     RARRAY(385) = 1.E-10,
19     RHSCAL = 0.,    U2STRS = 1.,     RHOIM = 1.0,
20     C4EDSW = .03,   OSUSQ = 1.E-4,
21     SIMPLT =1.E-5,  TMULT = 1.21,    EFMULT = .01,    ALC = 1.0,
22     TO = 1.0E-5,    TD = 10.0,       DELP = 20.,      HSINIT = 1.E-4,
23     CHIEPS =1.E-4,  HMAX = 4.0,
24 &END
```

Line	Command	
14	&NAME02	Real Namelist Data
15	UINF	Velocity non-dimensionalizing factor
	TOFINF	Temperature non-dimensionalizing factor
	REFL	Length non-dimensionalizing factor
16	GUMULT	If 1.0 use U2, U3 from continuity for right side of U2´, U3´ equations
17	OSG	Add stresses to RHS in p_p equation
18	VLDMLT	Use laminar diffusion in U_2' , U_3' equation
	VCMULT	Add convection to U_2', U_3' equations
	RARRAY(385)	Add convection to U_1' equations
19	RHSCAL	Add non-symmetric terms to Reynolds stresses
	U2STRS	Add stress terms to right side of p_p equations
	RHOIM	Adds wall damping to k, ε
20	C4EDSW	Integration station where ITKE flag is turned on
	OSUSQ	TKE minimum
21	SIMPLT	Station to begin implicit integration
	TMULT	Implicit step size = $\sqrt{TMULT}$
22	TO	Initial integration station
	TD	Downstream distance to final station
	DELP	Percent of TD for print
	HSINIT	Initial integration step size
23	CHIEPS	Convergence test on Newton Iteration
	HMAX	Maximum step size allowed
24	&END	End of Namelist real data

III. DYNAMIC ARRAY DIMENSIONING AND DEPENDENT VARIABLE SPECIFICATION

```
25FEDIMN              T  ALLOCATE STORAGE FOR ARRAYS
26IPINT   -1          T  DEPENDENT VARIABLE STORAGE ALLOCATION
27  1 2 3 5 6 7 8 9 0 0,  0 0 0 7*0,  10*I1 1  T
```

Line	Command	
25	FEDIMN	Dimension arrays to fit problem size
26	IPINT	Cards following specify dependent variable and parameter arrays

Variable 1 primary flow velocity

        2 Secondary flow velocity (vertical)

        3 Secondary flow velocity (horizontal)

        5 Turbulence kinetic energy

        6 Dissipation function

        7 Perturbation pressure (p_p)

        8 Complementary pressure (p_c)

        9 Continuity equation potential (ϕ_1)

Dependent variables and parameter arrays are stored in sequential arrays each of which is NODE long

In _NAME01_

    NDP is the number of arrays for space allocation

    NEQ is the number of equations to be integrated

    NEQADD is the number of equations to begin integrating following initialization

IV FLOWFIELD GEOMETRY, Non-Dimensionalization and Finite Element Matricies

```
28LINK2      14            T  GEOMETRY (DSCRTZ)
29VX1SCL                   T  ABCISSA COORDINATES
30  0.0,  4  .1  .8,  6  .6  1.25,  2  1.  1.   T
31VX2SCL                   T  ORDINATE COORDINATES
32  0.0,  2  .4  1.0,  6  .9  .8,  4  1.  1.25,  4  1.1  .8,  6  1.6  1.25,  2  2.0  1.0  T
33NDECRD                   T  DISCRETIZATION (X1,X2)
34   1  25,   1   13   0    T
35ELEM            0  0  13    T  ELEMENT CONNECTION TABLE
36DONE                     T  END GEOMETRY
37LINK3       4            T  COMPUTE NON-DIM. CONSTANTS. (DIMEN)
38LINK1       3            T  FINITE ELEMENT MATRICIES (GEOMFL)
```

Line	Command	
28	LINK2 14	Reads discretization data and generates triangular Finite Elements
29,30	VX1SCL	Abcissa Coordinates
31,32	VS2SCL	Ordinate Coordinates
33,34	NDECRD	Number of nodes in the Abcissa direction
		Number of nodes in the Ordinate direction
35	ELEM	Element connection table
36	DONE	End discretization
37	LINK3 4	Form non-dimensionalizing parameters
38	LINK1 3	Computes Finite Element matrices

secondary flow plane $[(x_3,x_2),(\bar{u}_3,\bar{u}_2)]$
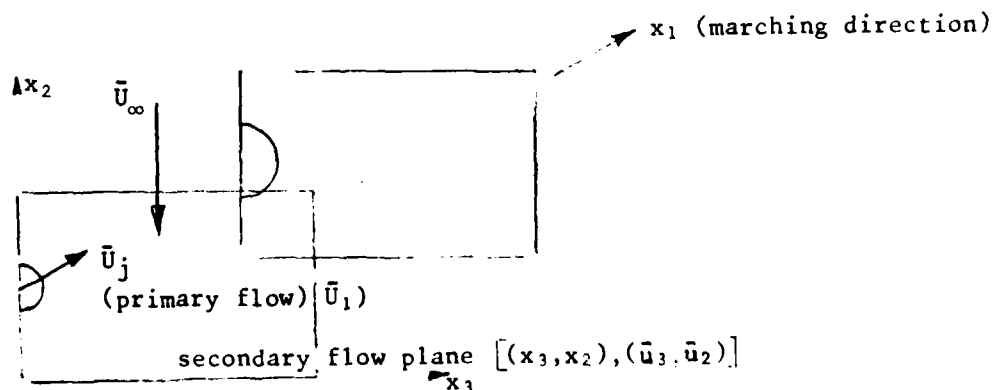
V. TITLES AND HEADINGS

```
39COMTITLE             T  READ TITLE FOR COMOC SYMBOL PAGE.
40DONE
41DESCRIPT  204        T  TITLE FOR EACH OUTPUT-HEADER PAGE
42
43        CIRCULAR JET IN CROSSFLOW. - - - 3DPNS
44
45DONE
46DESCRIPT  332        T  PARAMETER TITLES FOR OUTPUT.   (IOPAR)
47 REFERENCE           ENGLISH-FT       ENGLISH-IN       M-K-S              C
48 LENGTH              ...FEET...       ....IN....       ....M.....         ...
49 VELOCITY            ..FT/SEC..                        ...M/S....         ...
50 DENSITY             .LBM/FT3..                        ..KG/M3...         ...
51 TEMPERATURE         .RANKINE..                        ..KELVIN..
52 ENTHALPY            .BTU/LBM..                        ..KJ/KG...
53 FROZ.SPEC.HEAT      .BTU/LBM-R                        .KJ/KG-K..
54 VISCOSITY           .LBM/FT-S.                        .NT-S/M2..         ..P
55 LOCAL PRESSURE      ...PSF....       ...PSI....       ..NT/M2...         ...
56 ...CPU TIME...      .MACH. NO.       ..DPDX1...       ..ENERGY..         .CON
57 NWGEOM H'S          ...H21....       ...G22....       ...G23....         ...
58 X1/LREF             .DX1/LREF.       .EPSILON..       .DX1H/LREF REFL REY
59DONE
60MPARA    -1          T  SCALAR MULTIPLIERS FOR DIMENSIONING IONUMB
61                     T  (LOCATIONS IN RARRAY)
62                     5*2, 2*2 162 164 163, 3*2 164 163, 3*2 170 174,
63                     3*2 165 2, 2 -175 3*2, 3*2 176 2, 3*2 177 178,
64                     2  2  169 168 167,  3*2  108  2,  5*2, 5*2   T
65IONUMB   -1          T  PARAMETERS TO PRINT UNDER TITLES
66                     T  (LOCATIONS IN RARRAY)
67                     999, 5*200, 999, 200 4*43, 200 27 200 2*27,
68                     200 10 200 2*10, 200 58 200 58 200,
69                     200 97 200 97 200, 200 30 200 30 200,
70                     200  38  200  2*38,  999,  39  4*36,
71                     300 154  100 135  122,
72                     200 186 187 188 379, 11  12  14  85   47  T
73DESCRIP T   203      T  TITLES FOR PRINTED ARRAYS (IFMTHD)
74U1 / UREF            U2 / UREF        U3 / UREF        PHI            NU / NUR
EF * RE
75TKE /TKEREF          EPS / EPSREF     PP / PSTAG       U1 PRIME           PC
76PPRES                DPDX
77DONE
78IOSAVE  -1           T  ARRAYS TO BE PRINTED.  (CODED ADDRESSES).
79  1248 2248 3248 9248 1247,  5248 6248 7248 3301 8248  T
80IOMULT  -1           T  SCALAR MULTIPLIERS FOR EACH ARRAY PRINTED.
81                     4*2 21 5*2,  10*1  T
```

Line	Command	
39	COMTITLE	Problem identifying titles
41	DESCRIPT 204	Std print titles
46	DESCRIPT 332	Std output header labels
60	MPARA	Scalar parameter print multipliers
65	IONUMB	Scalar parameter print locations
73	DESCRIPT 203	Dependent variable print labels
78	IOSAVE	Dependent variable print locations*
80	IOMULT	Dependent variable print multipliers (RARRAY LOC.)

*Note in line 79 that the dependent variables are identified by decoding each number specified (ie. 1248 is stored in the first NODE locations beginning at the address in IZ(248); Variable 2, 2248, is directly behind Variable 1 since it is stored in the second NODE locations beginning at the address stored in IZ(248); etc.).

VI. DEPENDENT VARIABLE AND PARAMETER BOUNDARY RELATIONS*

```
82KBNO      1
83TOP               -RIGHT      2     DONE
84KBNO      2
85TOP               DONE
86KBNO      3
87LEFT              TOP                DONE
88KBNO      5
89ADD               DONE
90                  325*I1   1    T
91KBNO      6
92ADD               DONE
93                  325*I1   1    T
94KBNO      7
95TOP               -RIGHT      2     -BOTTOM      2     DONE
96KBNO      9
97TOP               -RIGHT      2     -BOTTOM   ,  2     DONE
```

Line	Command	
82	KBNO 1	Nodes where U_1 is held constant at initial values (Wall Nodes)
84	KBNO 2	Nodes where U_2 is fixed at initial values
86	KBNO 3	Nodes where U_3 is fixed at initial values
88	KBNO 5	Turbulence kinetic energy fixed at initial state
91	KBNO 6	Dissipation function fixed at initial state
94	KBNO 7	Perturbation pressure fixed at initial state
96	KBNO 9	Continuity potential function fixed at initial state

Named-side cards are formatted [4(A8, I8, 4X)]

Boundary conditions are applied to secondary flow plane.

Positive direction is counter-clockwise (ie. [-RIGHT 2] fixes the right column and node numbers. Node numbers are stored beginning at the second row from the top and proceeding toward the bottom row).
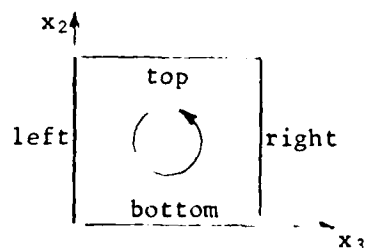
VII. PRIMARY FLOW TABLE DATA

```
98VU2POS    -3
99          0.  0.0166667  0.166667   T
100VU2VAL   136          T  NORMALIZED G2,G1 COORDINATES
101         .5  .5  .5    T
102VU3POS   -3
103         0.  0.0166667  0.166667   T
104VU3VAL   136          T  NORMALIZED F2,F1 COORDINATES
105         1.  1.  1.    T
106VX3ST    43           T  PRESSURE TABLE DOWNSTREAM STATIONS
107                         21*10.05  0.0   T
108VPVSX                 T  PRESSURE TABLE (PSF).
109                         21*2116.8   T
```

Line	Command	
98	VU2POS	Primary flow direction coordinates (X_1) where X_2 secondary flow plane geometry transformation is defined
100	VU2VAL	Expansion factors for variable X_2 coordinates
102	VU3POS	Primary flow direction coordinates (X_1) where X_3 secondary flow plane geometry transformation is defined
104	VU3VAL	Expansion factor for variable X_3 coordinates
106	VX3ST	Complementary pressure data stations
108	VPVSX	Complementary pressure (PSF)

Geometry Transformation

$$\eta_i = \left\{ \begin{array}{c} x_1 \\ \dfrac{x_2 - f_{21}(x_1)}{[f_{22}(x_1) - f_{21}(x_1)]/f_2} \\ \dfrac{x_3 - f_{31}(x_1)}{[f_{32}(x_1) - f_{31}(x_1)]/f_3} \end{array} \right\}$$

$f_{22}(x_1)$ and $f_{32}(x_1)$ are the span of the secondary plane

$f_{21}(x_1)$ and $f_{31}(x_1)$ are the minimum secondary plane coordinates

x_2 and x_3 are the coordinates of each grid point in respective directions

f_2 and f_3 are the secondary plane normalizing lengths

VIII. SOLUTION INITIATION

```
110LINKCALL   -1           T  SUBROUTINES CALLED AT END OF QKNUIN.
111                    5  12   T  PUNCH DATA HEN LPUNCH .GT. 0
112LINK1      2            T  GLOBAL NODAL-ELEMENT CONNECTIONS
113RARRAY         39  1.0
114VYY
115               78*.2  7*.4  6*.2  6*.8  .4  6*.2
.116               9(  5*1.  .8  .4  6*.2
117               6*.8  .4  6*.2  7*.4  6*.2  78*.2   T
118VYYEND      1
119VYY
120                         325*0.005  T
121VYYEND      5
122VYY        -
123                         325*0.012  T
124VYYEND      6
125RARRAY         95  0.0012
126RARRAY        271  0.0005
127READ  5 0 56 660    T   INITIALIZE OMEGA ARRAY
128                         325*1.0  T
129LINK1      4            T  INITIALIZE DEP. VAR.
130LINK5      6            T  SET NU TURBULENT LEVELS.  (DFCFBL)
131IARRAY    97     0  T  RESET ITKE
132QKNINT                 T  BEGIN INTEGRATION.
133EXIT                   T  TERMINATE RUN.
134CASE END               T  LAST DATA CASE
```

Line	Command		
112	LINK 1	2	Form global nodal-element connection array
113	RARRAY	39	Non-dimensional global pressure level
114	VYY	1	Initial primary velocity distribution
119	VYY	5	Initial turbulence kinetic energy distribution
122	VYY	6	Initial dissipation function distribution
125	RARRAY	95	Minimum value allowed for dissipation function
126	RARRAY	271	Minimum value allowed for turbulence kinetic energy
127	READ	56	Initialize the wall damping array
129	LINK 1	4	Initialize the dependent variables
130	LINK 5	6	Initialize NU turbulent levels
131	IARRAY	97	Reset ITKE to zero
132	QKNINT		Initiate implicit Newton integration
133	EXIT		Terminate run and return for next data case
134	CASE END		Last data case

```
101C            - - - C - O - M - O - C - - -
102C
103       COMMON / NPINTQ / JJJ(30)
104C
105       COMMON / VARBLE / IARRAY(00500), RARRAY(00500)
106       EQUIVALENCE ( IARRAY(00092), IZSIZE )
107       COMMON / ARRAYS / IZ(130000)
108       NZSIZE  =  130000
109C
110C -- IBM ERROR HANDLER
111C      CALL ERRSET ( 207, 500, -1, 1, 0, 217 )
112 100   CONTINUE
113       CALL ZEROTA
114       CALL RESET ( 00500, IARRAY, 0 )
115       CALL RESET ( 00500, RARRAY, 0.0 )
116       IZSIZE  =  NZSIZE
117       CALL RESET  ( IZSIZE, IZ, 0 )
118       CALL BDINPT
119       GO TO 100
120       END
121       SUBROUTINE GETPPR
122       COMMON / ARRAYS / IZ(1)
123       DIMENSION  RZ(1), L(400)
124       EQUIVALENCE  ( RZ(1), IZ(1), L(1) )
125       EQUIVALENCE (L(026),IINODE),(L(109),IB112 ),(L(110),IB113 )
126       EQUIVALENCE (L(077),IAREA ),(L(036),IIELS )
127       EQUIVALENCE (L(089),IX1COR),(L(090),IX2COR)
128       COMMON / NPINTQ / JU, JV, JW, JH, JK, JE, JP, JS, JT, JAD(21)
129       COMMON / JADRES / JUAD, JVAD, JWAD, JHAD, JKAD, JEAD, JPAD, JSAD
130      1 , JEXT(22)
131       COMMON /VARBLE/  IARRAY(500), RARRAY(500)
132       EQUIVALENCE ( IARRAY(00014), NELEM  )
133       EQUIVALENCE ( IARRAY(00016), NNODE  )
134       EQUIVALENCE ( IARRAY(00191), NM     )
135       EQUIVALENCE ( RARRAY(00027), UINF   )
136       EQUIVALENCE ( RARRAY(00314), C4     )
137       DATA  NT / 0 /
138C
139       IF ( NT .GE. 2 ) RETURN
140       UNON    =  0.10
141       UMAX    =  0.4
142       UMIN    =  0.20
143       YB      =  RZ(IX2COR+156)
144       ZB      =  RZ(IX2COR+104)
145       A       =  1.01 * ( YB - ZB )
146       ASQ     =  A * A
147C
148C -- INITIALIZE DEPENDENT VARIABLE ARRAYS
149C --    (NON-DIMENSIONAL)
150C
151C      JUAD = U1
152C      JVAD = U2
153C      JWAD = U3
154C      JKAD = TKE
155C      JEAD = DISSIPATION
156C
157       DO 200 I = 1, NNODE
158       IM      =  I - 1
159       Y       =  RZ(IX2COR+IM) - YB
160       Z       =  RZ(IX1COR+IM)
161       RSQ     =  Y * Y + Z * Z
162       RZ(JSAD+IM)  =  1.0
163       IF ( RSQ .LT. ASQ ) GO TO 200
164       R       =  SQRT(RSQ)
165       THETA   =  ASIN(Y/R)
166       COS2TH  =  COS(2.0*THETA)
167       SIN2TH  =  SIN(2.0*THETA)
168       ASR     =  ASQ / RSQ
169       UVEL    =  ASR * ASR
170       IF ( UVEL .LT. UMAX ) UVEL = UMIN
171       RZ(JUAD+IM)  =  UVEL
172       RZ(JVAD+IM)  =  -UNON * ( ASR*COS2TH + 1.0 )
173       RZ(JWAD+IM)  =  UNON * SIN2TH * ASR
174       RZ(JKAD+IM)  =  0.1 * RZ(JKAD+IM)
175       RZ(JEAD+IM)  =  0.1 * RZ(JEAD+IM)
176 200   CONTINUE
177       RETURN
178       END
```

```
179       SUBROUTINE NODPPR
180       COMMON / JADRES / JUAD, JVAD, JWAD, JHAD, JKAD, JEAD, JPAD, JSAD
181      1 , JEXT(22)
182C
183       COMMON / ARRAYS / IZ(1)
184       DIMENSION  RZ(1), L(400)
185       EQUIVALENCE ( IZ(1), RZ(1), L(1) )
186       EQUIVALENCE (L(105),IPRGRD)
187C
188       COMMON / VARBLE / IARRAY(00500), RARRAY(00500)
189C
190       EQUIVALENCE ( IARRAY(00016), NNODE  )
191       EQUIVALENCE ( IARRAY(00086), KPNT   )
192       EQUIVALENCE ( IARRAY(00304), NELPAS )
193       EQUIVALENCE ( IARRAY(00312), IUONLY )
194       EQUIVALENCE ( IARRAY(00396), JNCPRG )
195C
196       EQUIVALENCE ( RARRAY(00023), TIME   )
197       EQUIVALENCE ( RARRAY(00062), CONV   )
198       EQUIVALENCE ( RARRAY(00100), PPRIME )
199       EQUIVALENCE ( RARRAY(00207), CONVRG )
200       EQUIVALENCE ( RARRAY(00208), AMSDIF )
201       EQUIVALENCE ( RARRAY(00347), TSCALE )
202       EQUIVALENCE ( RARRAY(00385), UCMULT )
203       EQUIVALENCE ( RARRAY(00398), T2PFIX )
204C
205 9600 FORMAT ( 1H ,   6H PASS , I4,   1H, I3, 12H ITERATIONS. ,
206      1 9H STATION , 1PE13.5 )
207C
208       IUONLY  =   3
209       NVERG   =   CONVRG
210       STAT    =   TIME * CONV
211       NPASP1  =   NELPAS
212       WRITE ( 6, 9600 ) NPASP1, NVERG, STAT
213C
214C -- GRID EXPANSION (CONTRACTION)
215C
216       CALL NWGEOM
217C
218       IF ( JNCPRG .EQ. 1 ) CALL JNCPPR
219       AMSDIF  =  PPRIME
220C
221C -- INCREASE PRESSURE EFFECT TO 100% OVER TEN STEPS
222C
223       IF ( NELPAS .LT. 9 ) UCMULT = 1.0E-10
224       IF ( NELPAS .LT. 9 ) GO TO 100
225       UCMULT  =  UCMULT + 0.1
226       IF ( UCMULT .GT. 1.0 ) UCMULT = 1.0
227 100  CONTINUE
228       DO 200 I = 1, NNODE
229       IM       = I - 1
230       RZ(JSAD+IM)  =  1.0 - 0.5 * ( RZ(JWAD+IM)**2 + RZ(JVAD+IM)**2 )
231       RZ(IPRGRD+IM)  =  UCMULT * RZ(IPRGRD+IM)
232 200  CONTINUE
233       RETURN
234       END
```

AIRCRAFT AND CREW SYSTEMS TECHNOLOGY DIRECTORATE

DISTRIBUTION LIST

Commander
Naval Weapons Center
China Lake, CA 93555

Director
National Aeronautics & Space Administration
Ames Research Center
Moffett Field, CA 94035
Attn: S.. Anderson

Commanding Officer
Naval Air Propulsion Center
Trenton, NJ 08628

Director
National Aeronautics & Space Administration
Flight Research Center
Edwards Air Force Base, CA 93523

Commander
Naval Air Test Center
Patuxent River, MD 20670

Director
National Aeronautics & Space Administration
Langley Research Center
Hampton, CA 23365

Commander
David Taylor Naval Ship Research
  & Development Center
Bethesda, MD 20034

Director
National Aeronautics & Space Administration
Lewis Research Center
21000 Brooke Park Road
Cleveland, OH 44135

Chief
Office of Naval Research
800 N. Quincy Street
Arlington, VA 22217

Director
Air Force Flight Dynamics Laboratory
  (ASD/ENFDH)
Wright-Patterson Air Force Base
Dayton, OH 45433

Institute of Defense Analysis
400 Army Navy Drive
Arlington, VA 22202
Attn: J. Attinello

Commander
Air Force Aeronautical Systems Division
Wright-Patterson Air Force Base
Dayton, OH 45433

Superintendent
Naval Postgraduate School
Monterey, CA 93940

Commander
Air Force Flight Test Center
Edwards Air Force Base, CA 93523

Commanding Officer
Army Aviation Systems Test Activity
Edwards Air Force Base, CA 93523

Administrator
Defense Documentation Center for
  Scientific & Technical Information (DDC)
Building #5, Cameron Station
Alexandria, VA 22314
(12 copies)

Commanding General
Army Aviation Systems Command
St. Louis, MO 63102

Office of Naval Research
800 N. Quincy Street
Arlington, VA 22214
Attn: Dr. R. Whitehead

Commander
Naval Air Systems Command (AIR-954)
Department of the Navy
Washington, DC 20361
(7 copies: (2) for retention
            (2) for AIR-320D
            (1) for AIR-5301
            (1) for PMA-257
            (1) for AIR-03PA)

Commander
Naval Air Development Center
Warminster, PA 18974
(13 copies: (3) for Code 813
            (10) for Code 6053)

General Dynamics
Convair Division
P.O. Box 80986
San Diego, CA 92138

McDonnell Douglas Corporation
3855 Lakewood Boulevard
Long Beach, CA 90808

McDonnell Douglas Corporation
P.O. Box 516
St. Louis, MO 63166

Pratt & Whitney Aircraft Division
Division of United Aircraft Corporation
East Hartford, CT 06108

Lockheed California Company
P.O. Box 551
Burbank, CA 91503

Northrop Corporation
Hawthorne, CA 90250

The Boeing Company
Seattle, WA 98101

Lockheed-Georgia Company
Marietta, GA 30061

LTV Aerospace Corporation
Dallas, TX 75221

Grumman Aerospace Corporation
Bethpage, Long Island, NY 11714

Rockwell International
Columbus, OH 43216

General Dynamics Corporation
Ft. Worth, TX 76108

Rockwell International
Los Angeles, CA 90053

Hughes Aircraft Company
Culver City, CA 90230

Fairchild-Republic Corporation
Farmingdale, Long Island, NY 11735

DATE
ILME